

The Electromagnetic Signals of Compact Binary Mergers

Tsvi Piran¹, Ehud Nakar² and Stephan Rosswog^{3,4,5}

¹*Racah Institute of Physics, The Hebrew University, Jerusalem 91904, Israel*

²*Raymond and Beverly Sackler School of Physics & Astronomy, Tel Aviv University, Tel Aviv 69978, Israel*

³*School of Engineering and Science, Jacobs University Bremen, Germany*

⁴*TASC, Department of Astronomy and Astrophysics, University of California, Santa Cruz, CA 95064*

⁵*Astronomy and Oskar Klein Centre, Stockholm University, AlbaNova, SE-10691 Stockholm, Sweden*

8 January 2013

ABSTRACT

Compact binary mergers are prime sources of gravitational waves (GWs), targeted by current and next generation detectors. The question “what is the observable electromagnetic (EM) signature of a compact binary merger?” is an intriguing one with crucial consequences to the quest for gravitational waves. We present a large set of numerical simulations that focus on the electromagnetic signals that emerge from the dynamically ejected sub-relativistic material. These outflows produce on a time scale of a day macronovae - short-lived IR to UV signals powered by radioactive decay. Like in regular supernovae the interaction of this outflow with the surrounding matter inevitably leads to a long-lasting remnant. We calculate the expected radio signals of these remnants on time scales longer than a year, when the sub-relativistic ejecta dominate the emission. We discuss their detectability in 1.4 GHz and 150 MHz and compare it with an updated estimate of the detectability of short GRBs’ orphan afterglows (which are produced by a different component of this outflow). We find that mergers with characteristics similar to those of the Galactic neutron star binary population (similar masses and typical circum-merger Galactic disk density of $\sim 1 \text{ cm}^{-3}$) that take place at the detection horizon of advanced GW detectors (300 Mpc) yield 1.4 GHz [150 MHz] signals of ~ 50 [300] μJy , for several years. The signal on time scales of weeks, is dominated by the mildly and/or ultra-relativistic outflow, which is not accounted for by our simulations, and is expected to be even brighter. Upcoming all sky surveys are expected to detect a few dozen, and possibly more, merger remnants at any given time thereby providing robust lower limits to the mergers rate even before the advanced GW detectors become operational. The macronovae signals from the same distance peak in the IR to UV range at an observed magnitude that may be as bright as 22–23 about 10 hours after the merger but dimmer, redder and longer if the opacity is larger.

1 INTRODUCTION

Compact binary (neutron star - neutron star, ns^2 , or black hole - neutron star, nsbh) mergers are prime sources of gravitational radiation. The GW detectors LIGO (Abbott et al. 2009a), Virgo (Acernese et al. 2008) and GEO600 (Grote & the LIGO Scientific Collaboration 2008) are designed to optimally detect merger signals. These detectors have been operational intermittently during the last few years reaching their nominal design sensitivity (Abbott et al. 2009b; Sengupta et al. 2010; the LIGO Scientific Collaboration & the Virgo Collaboration 2010) with detection horizons of a few dozen Mpc for ns^2 and almost a hundred Mpc for nsbh mergers (the LIGO - Virgo collaboration adopts an optimal canonical distance of 33/70 Mpc; Abadie et al. 2010). Both LIGO and Virgo are being upgraded now and by the end of 2015 are expected to be operational at sensitivities $\sim 10 - 15$ times greater than the initial LIGO (Smith & LIGO Scientific Collaboration

2009), reaching a detection horizon of a few hundred Mpc for ns^2 mergers and about a Gpc for nsbh mergers (445/927 Mpc are adopted by the LIGO-Virgo collaboration as canonical values; Abadie et al. 2010).

Understanding the observable EM signature of compact binary mergers has several observational implications. First, once the detectors are operational it is likely that the first detection of a GW signal will be around or even below threshold. Detection of an accompanying EM signal will confirm the discovery, thereby increasing significantly the sensitivity of GW detectors (Kochanek & Piran 1993; Hughes & Holz 2003; Dalal et al. 2006; Arun et al. 2009). Second, the physics that can be learned from observations of a merger event through different glasses is much greater than what we can learn through EM or GW observations alone. Finally, even before the detectors are operational, the detection of EM signatures will enable us to determine the

merger rates¹, an issue of utmost importance for the design and the operation policy of the advanced detectors.

The electromagnetic signal that is often considered as the most promising counterpart to gravitational waves is that of short Gamma-Ray Bursts (GRBs), which are thought to arise from compact binary merger events (Eichler et al. 1989). The estimated rate of short GRBs is indeed comparable to binary pulsar estimates (Guetta & Piran 2006; Nakar et al. 2006; Guetta & Stella 2009). However, while appealing, the association is not proven yet (Nakar 2007), and even if there is an association, short GRBs are observed only if their relativistic jets points towards us. If short GRBs are binary mergers then their observed rate, $\sim 10 \text{ Gpc}^{-3} \text{ yr}^{-1}$, provides a lower limit to the merger rate. The true rate is higher and it depends on the poorly constrained beaming angle, which results in an uncertainty of almost two orders of magnitude. While a GRB that is observed off-axis is undetectable in gamma-rays, it produces a long-lasting radio “orphan” afterglow, which may be detectable (Rhoads 1997; Waxman et al. 1998; Frail et al. 2000; Levinson et al. 2002; Gal-Yam et al. 2006). A key point in estimating the detectability of GRB orphan afterglows is that the well constrained observables are the *isotropic* equivalent energy of the flow and the rate of bursts that point towards earth. However, the detectability of the orphan afterglows depends only on the *total* energy and *true* rate, namely on the poorly constrained jet beaming angle. Levinson et al. (2002) have shown that while narrower beaming increases the true rate it reduces the total energy, and altogether reduces the detectability of radio orphan afterglows. This counterintuitive result makes the detectability of late emission from a decelerating jet, which produced a GRB when it was still ultra-relativistic, less promising.

Regardless of the amount of ultra-relativistic outflow that is launched by compact binary mergers, and of whether they produce short GRBs or not, mergers do launch energetic sub-relativistic and mildly-relativistic outflows (e.g., Rosswog et al. 1999; Ruffert & Janka 2001; Rosswog 2005; Rosswog & Price 2007; Yamamoto et al. 2008; Rezzolla et al. 2010), unless the equation of state at supra-nuclear densities is extremely soft (Rosswog et al. 2000a). Recently, Nakar & Piran (2011) showed that the interaction of these outflows with the surrounding matter will inevitably produce radio counterparts. An additional source of electromagnetic signal was suggested by Li & Paczyński (1998), which argue that the freshly synthesized, radioactive elements in the ejected debris from the merger will

drive a short-lived supernova-like event often referred to as “macronova” (Kulkarni 2005). Metzger et al. (2010) find that if $0.01 M_{\odot}$ is ejected then the optical emission from a merger at 300 Mpc peaks after ~ 1 day at $m_V \approx 23$ mag. For a recent discussion of the detectability of the various electromagnetic counterparts of GW sources see Metzger & Berger (2012).

In addition to electromagnetic signals, there will be a strong ($\sim 10^{53}$ erg) burst of ~ 10 MeV neutrinos, similar to what is produced by a core-collapse supernova. But since compact binary mergers are orders of magnitude rarer than supernova events, the chances of detecting neutrinos from a cosmological merger event are essentially zero.

In a companion paper (Rosswog et al. 2012; in the following called “paper I”) we have investigated to which extent dynamical collisions as they occur, for example, in a globular cluster are different from a gravitational wave driven compact binary merger. In this paper we concentrate entirely on binary mergers and we systematically explore the neutron star binary parameter space in a large set of simulations. We use numerical simulations of the merger process to find the properties of the dynamically ejected outflow for different masses of the coalescing compact stars. We then take the resulting ejecta profiles and calculate the electromagnetic transients (i.e., radio flares and macronovae) that are related to the dynamical ejecta of ns^2 and nsbh binaries.

Our study does not account for other types of outflows such as neutrino-driven winds (which yield moderate velocities of $\sim 0.1 c$; Dessart et al. 2009) or mildly and/or ultra-relativistic outflows that may emerge from close to the compact object at the center of the merger. Since only the sub-relativistic dynamically ejected material is explored we restrict the light curve calculation to time scales of a year and longer, when the sub-relativistic component dominates the emission. On shorter time scales of weeks and months the mildly relativistic component dominates. Since the radio luminosity depends strongly on the outflow velocity, emission on time scales of weeks and months will be brighter than the one that we find here even if the mildly relativistic component carries a small fraction out of the total outflow energy (see Nakar & Piran 2011 for details). The radio flares depend sensitively on the surrounding ISM density. We focus here on physical parameters found in known Galactic ns binaries. Since all known binaries reside in the Galactic disk, we consider a uniform density of 1 cm^{-3} Draine (2011) as the most likely circum-merger environment².

Our new simulations, that focus on the ejecta also enable us to revise the estimates of the macronovae light curves. These light curves are determined mostly by three ingredients: (i) the total amount of the ejecta and their velocity structure that we calculate here; (ii) the energy input from radioactive decay, for which we use the most accurate estimates to date by Korobkin et al. (2012) and (iii) the (poorly known) material opacity, taken from Metzger et al. (2010). At a finer level the light curve and the peak luminosity depend also on the velocity distribution as the emission

¹ The current rate constraints on compact binary mergers are rather loose. The last LIGO and Virgo runs provided only weak upper limits on the merger rates: $1.4 \times 10^4 \text{ Myr}^{-1} (10^{10} L_{\odot})^{-1}$ corresponding to $\sim 2 \times 10^5 \text{ Gpc}^{-3} \text{ yr}^{-1}$ for ns^2 and $3600 \text{ Myr}^{-1} (10^{10} L_{\odot})^{-1}$ ($\sim 5 \times 10^4 \text{ Gpc}^{-3} \text{ yr}^{-1}$) for nsbh (Abbott et al. 2009b). Estimates based on the observed binary pulsars in the Galaxy are highly uncertain, with values ranging from $20 - 2 \times 10^4 \text{ Gpc}^{-3} \text{ yr}^{-1}$ (Phinney 1991; Narayan et al. 1991; Kalogera et al. 2004a,b; Abadie et al. 2010). There are no direct estimates of nsbh mergers, as no such system has ever been observed, and here one has to rely only on a parameter dependent population synthesis (e.g., Belczynski et al. 2008; Mandel & O’Shaughnessy 2010).

² Ns^2 binaries are in random locations in the Galactic disk. Draine (2011) estimates that 0.4 of the disk volume has a density of about 0.6 cm^{-3} , 0.1 of the volume has a much higher density while the rest has a low density.

from a given mass element moving with a specific velocity peaks when this element becomes optically thin. We use the simulation results to estimate this time scale and in this way we obtain macronovae light curves for our different merger cases.

We begin (§2) with a brief discussion of our numerical simulations (more details can be found in paper I). We focus in this discussion on the ejecta properties which are critical both for radio flares and for macronovae. In §3 we first provide an analytic calculation of the radio emission resulting from the interaction of single velocity ejecta with the surrounding interstellar matter (ISM). Then, we expand this solution to an outflow with a distribution of velocities and we present a semi-analytic calculation to find the signal resulting from the ejecta obtained in the simulations, which show a velocity range of 0.1-0.5 c . We discuss the observational implications for detectability of merger remnants in §4, including a comparison to an updated estimate of short GRB orphan afterglows detectability (§4.2). In §5 we present a general theory of a macronova light curve for a case with a velocity distribution within the ejecta. We use in these calculations new radioactive energy deposition rates calculated recently in a companion paper by Korobkin et al. (2012). We then present our detailed calculations of the expected IR to UV luminosity of macronovae that arise from radioactive decay within the outflow. We summarize our results and discuss their implications in §6.

2 NUMERICAL SIMULATIONS

Neutron stars (ns) have long been thought to be narrowly distributed around $1.35 m_{\odot}$ (Thorsett & Chakrabarti 1999). With an increasing number of observed systems it has, however, turned out that the mass range that is realized in nature is substantially broader. For example, there is now ample support for neutron star masses significantly larger than $1.5 m_{\odot}$ (see for example the data compilation in Lattimer & Prakash 2010). A broad peak around 1.5-1.7 m_{\odot} has been found (Kiziltan et al. 2010; Valentim et al. 2011) for neutron stars with white dwarf companions. In addition, there may be a low-mass peak of $\sim 1.25 m_{\odot}$ neutron stars that have been produced by electron capture supernovae (Podsiadlowski et al. 2004; van den Heuvel 2004; Schwab et al. 2010). PSR J1614-2230 with a mass of $1.97 \pm 0.04 m_{\odot}$ (Demorest et al. 2010) is nowadays considered as a robust lower limit on the maximum neutron star mass, but even neutron stars with considerably larger masses are not implausible.

These findings are more than enough of a motivation for a broad scan of the neutron star binary parameter space. We explore neutron star masses between 1.0 to 2.0 m_{\odot} in steps of 0.2 m_{\odot} . All our neutron stars have a negligible initial spin, consistent with the results of Bildsten & Cutler (1992) and Kochanek (1992). Our simulations make use of the Smooth Particle Hydrodynamics (SPH) method, see Monaghan (2005) and Rosswog (2009) for recent reviews. Our code is an updated version of the one that was used in earlier studies (Rosswog & Davies 2002; Rosswog & Liebendörfer 2003; Rosswog et al. 2003; Rosswog 2005). It uses the Shen et al. equation of state

(EOS) (Shen et al. 1998a,b), an opacity-dependent multi-flavor neutrino leakage scheme (Rosswog & Liebendörfer 2003) and a time-dependent artificial viscosity treatment, see Rosswog et al. (2000b, 2008) for details. In all nsbh simulations Newtonian gravity was employed and the black hole was vested with an absorbing boundary at the Schwarzschild radius. All simulations used a simple gravitational wave emission backreaction force (Davies et al. 1994). The performed simulations complement those that have been presented in Paper I. For completeness, we have also performed two simulations of neutron star black hole binary systems. Since we found in earlier studies (Rosswog et al. 2004) cases of long-lived, episodic mass transfer, we started the two cases with lower numerical resolution to be able to follow them until the neutron star is completely disrupted³. Our results have turned out to be very robust with respect to the numerical resolution, therefore the reduced numerical resolution is not a concern for the purpose of our study. The system parameters and some key properties of the ejecta are summarized in Table 1.

In all investigated cases we find $\sim 10^{-2} m_{\odot}$ of unbound material ($E_{\text{kin}} + E_{\text{pot}} > 0$). A deviation of the mass ratio from unity has the tendency to enhance the amount of ejected mass, we find in contrast no clear tendency with the total system mass, see column six in Table 1. In all cases the ejecta velocities are below 0.5 c , their mass-averaged values are given in column seven, they are typically close to 0.13 c .

Figs. 1 and 2 depict the remnant structures in the orbital (XY) plane and perpendicular to it (XZ) at the end of the simulations. Clearly, visible is the sensitivity to deviations from a mass ratio of unity: even differences of 15% in the stellar masses lead to large asymmetries, i.e. one pronounced tidal tail rather than a disk resulting from initially two such tails. The debris matter cannot cool rapidly enough, therefore it is puffed up, see Fig. 2, but at the end of the simulations far from spherical symmetry. Although this may lead to some viewing angle dependencies, we assume in the following for simplicity spherically symmetric outflows.

Compact binary mergers inevitably eject mass in various forms:

a) If compact binaries indeed power short GRBs, they have to launch ultra-relativistic outflows with Lorentz factors > 100 -1000. There are several mechanisms by which this could be achieved (e.g., Blandford & Znajek 1977; Hawley & Krolik 2006; Piran 2004; Lee & Ramirez-Ruiz 2007; Nakar 2007)

b) Once the merger has happened, the hot remnant emits a few times 10^{53} erg/s in ~ 20 MeV neutrinos (Eichler et al. 1989; Ruffert & Janka 2001; Rosswog & Liebendörfer 2003; Sekiguchi 2011). The peak of the neutrino emission is delayed with respect to the merger itself by the time it takes

³ Phases of stable mass transfer are not necessarily restricted to simulations that use the approximation of Newtonian gravity. Relativistic binary simulations with small mass ratios and large bh spin parameters may be particularly prone to a stable mass transfer phase, see Shibata & Taniguchi (2011) for a further discussion.

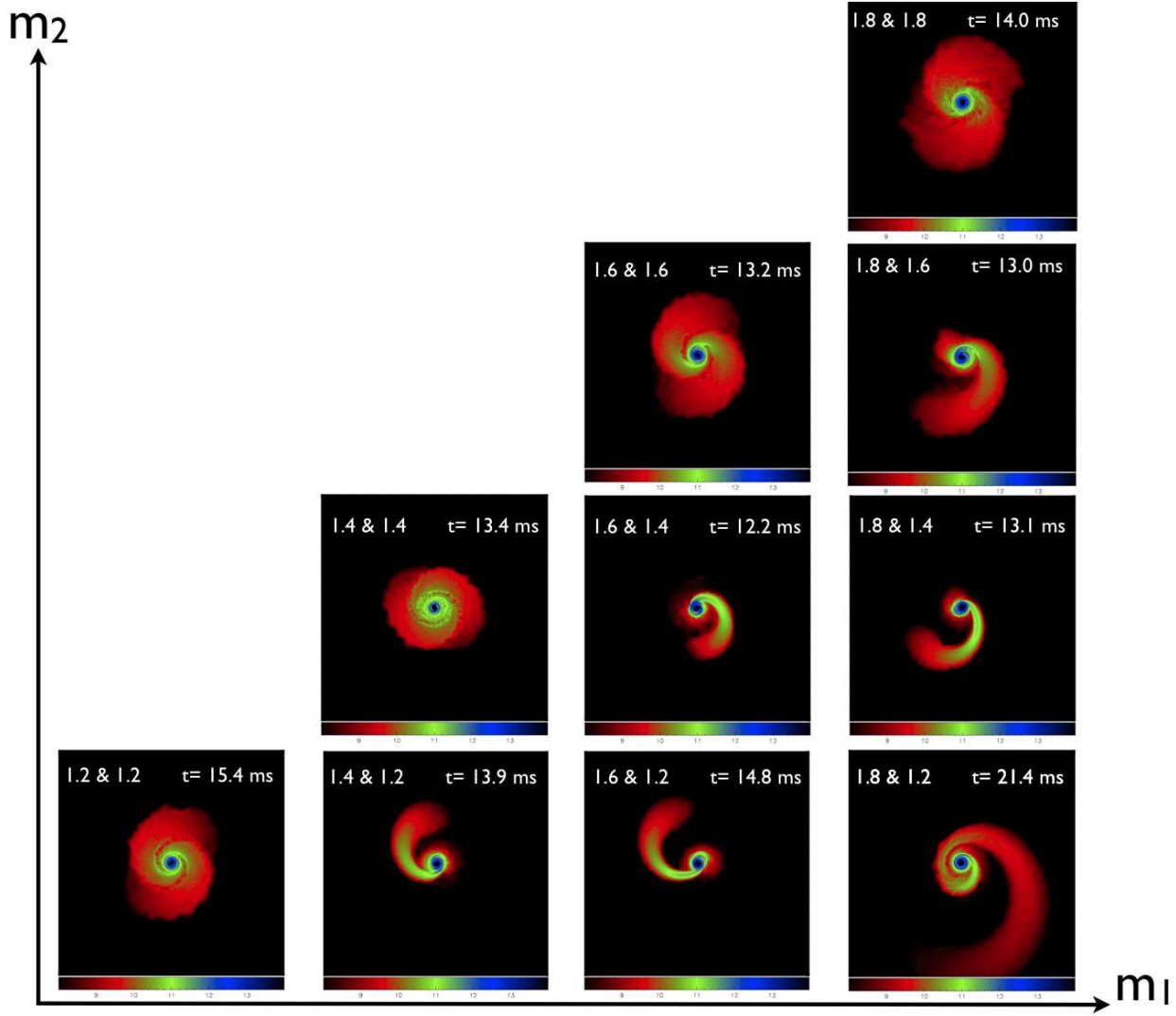


Figure 1. Density cuts through the orbital planes of all merger remnants at the end of each simulation. Each snapshot shows a region of 1000 km x 1000 km, color coded is the logarithm of mass density in g cm^{-3} , the annotations indicate the stellar masses (solar units) and the time of the snapshot.

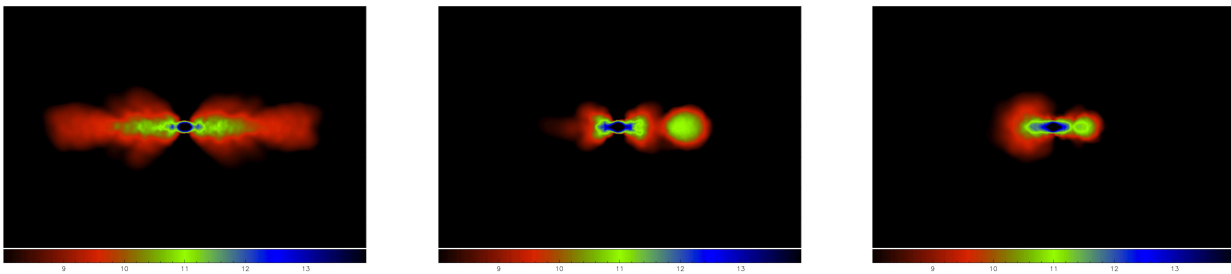


Figure 2. Density cuts (XZ-plane) at the last time slice of the simulations with $2 \times 1.4 m_{\odot}$ (left), 1.6 and $1.4 m_{\odot}$ (middle) and 1.8 and $1.4 m_{\odot}$ (right). The chosen cases correspond to the second line of panels (counted from below) in Fig. 1.

Table 1. Overview over the performed simulations

Run	$m_1 [m_\odot]$	$m_2 [m_\odot]$	$N_{\text{SPH}} [10^6]$	$t_{\text{end}} [\text{ms}]$	$m_{\text{ej}} [m_\odot]$	$\langle v_{\text{esc}} \rangle$	$E_{\text{kin}} [10^{50} \text{erg}]$
1	1.0	1.0	1.0	15.3	7.64×10^{-3}	0.10	1.0
2	1.2	1.0	1.0	15.3	2.50×10^{-2}	0.11	3.4
3	1.4	1.0	1.0	16.5	2.91×10^{-2}	0.13	4.8
4	1.6	1.0	1.0	31.3	3.06×10^{-2}	0.13	5.3
5	1.8	1.0	1.0	30.4 *	$> 1.64 \times 10^{-2}$	0.13	3.2
6	2.0	1.0	0.6	18.8 *	$> 2.39 \times 10^{-2}$	0.16	6.0
7	1.2	1.2	1.0	15.4	1.68×10^{-2}	0.11	2.3
8	1.4	1.2	1.0	13.9	2.12×10^{-2}	0.12	3.2
9	1.6	1.2	1.0	14.8	3.33×10^{-2}	0.13	6.2
10	1.8	1.2	1.0	21.4	3.44×10^{-2}	0.14	7.0
11	2.0	1.2	0.6	15.1 *	$> 2.95 \times 10^{-2}$	0.14	6.0
12	1.4	1.4	1.0	13.4	1.28×10^{-2}	0.10	1.6
13	1.6	1.4	1.0	12.2	2.36×10^{-2}	0.12	4.0
14	1.8	1.4	1.0	13.1	3.84×10^{-2}	0.14	7.6
15	2.0	1.4	0.6	15.0	3.89×10^{-2}	0.15	8.7
16	1.6	1.6	1.0	13.2	1.97×10^{-2}	0.11	2.9
17	1.8	1.6	1.0	13.0	1.67×10^{-2}	0.12	2.7
18	2.0	1.6	0.6	12.4	3.79×10^{-2}	0.14	7.6
19	1.8	1.8	1.0	14.0	1.50×10^{-2}	0.12	2.8
20	2.0	1.8	0.6	11.0	1.99×10^{-2}	0.13	3.7
21	2.0	2.0	0.2	21.4	1.15×10^{-2}	0.11	1.8
22	5+	1.4	0.2	138.7	2.38×10^{-2}	0.15	6.0
23	10+	1.4	0.2	139.3	4.93×10^{-2}	0.18	18.2

* The secondary is still orbiting at the end of the computations.

+ The primary is a black hole.

to form a hot accretion torus, about 10 ms. At these huge luminosities the neutrinos drive a strong baryonic wind of $\dot{M} \sim 10^{-3} m_\odot/\text{s}$ and $v \sim 0.1c$ (Dessart et al. 2009), preferentially in the direction of the rotation axis.

c) It is very likely that the outflows of process a) and b) interact near the rotation axis/the inner disk. Such an interaction plausibly produces moderately relativistic matter outflows near the jet-wind interface.

d) As the accretion disk evolves it spreads viscously until dissipational heating and/or the recombination of nucleons into nuclei unbind a large fraction of the late-time disk (Chen & Beloborodov 2007; Lee & Ramirez-Ruiz 2007; Metzger, Piro & Quataert 2008; Beloborodov 2008).

e) Gravitational torques dynamically eject matter directly at first contact with velocities $> 0.1 c$, see Tab. 1.

While all of the above mass loss processes undoubtedly occur, the quantitative calculation of processes a) to d) is technically very demanding and the relevant physical processes are not included in the presented simulations. We therefore do not consider here their contribution to the electromagnetic signature (which will be most important for the radio emission at early times - as discussed later). Instead, we focus entirely on the signature of the dynamic ejecta, which

can be reliably calculated⁴. Their properties are entirely set during the first contact and by the end of the simulation the unbound material is moving ballistically, with fast moving ejecta ahead of slower one. The ballistic motion ends only when the dynamical ejecta start being decelerated by the ambient material months-years after the merger (see below). The dynamically ejected debris is expected to be the most energetic of all the outflow components. As a result its velocity profile is not expected to be significantly affected by interaction with other outflow components and its profile at the end of the numerical simulation provides a good approximation of the initial conditions for the electromagnetic signal calculations.

3 THE RADIO SIGNAL FROM OUTFLOW-ISM INTERACTION

We begin by calculating analytically the radio signal resulting from a single velocity outflow and from an outflow with a

⁴ Note, that the presented ejecta amounts are numerically fully converged. They can, however, depend on the included physics ingredients such as the equation of state or the treatment of gravity (Newtonian vs. GR).

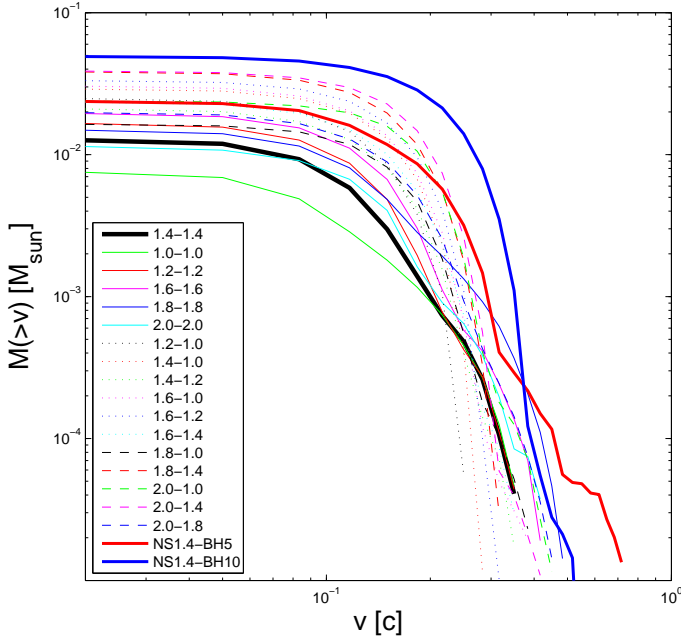


Figure 3. Ejected mass with energy above a given velocity for the different merger cases.

power-law velocity distribution. We begin in section §3.1 by repeating (for completeness) and extending the calculation discussed in the supplementary material of Nakar & Piran (2011). We then use semi-analytical calculations to generalize the result to ejecta with an arbitrary distribution of velocities.

3.1 A single velocity outflow

Consider a spherical outflow with an energy E and an initial Lorentz factor Γ_0 , with a corresponding velocity $c\beta_0$, that propagates into a constant density, n , medium. If the outflow is not ultra-relativistic, i.e., $\Gamma_0 - 1 \lesssim 1$ it propagates at a constant velocity until, at t_{dec} , it reaches radius R_{dec} , where it collects a comparable mass to its own (Nakar & Piran 2011):

$$R_{dec} = \left(\frac{3E}{4\pi n m_p c^2 \beta_0^2} \right)^{1/3} \approx 10^{17} \text{ cm } E_{49}^{1/3} n^{-1/3} \beta_0^{-2/3}, \quad (1)$$

and

$$t_{dec} = \frac{R_{dec}}{c\beta_0} \approx 30 \text{ day } E_{49}^{1/3} n^{-1/3} \beta_0^{-5/3}, \quad (2)$$

where we approximate $\Gamma_0 - 1 \approx \beta_0^2$ and ignore relativistic effects. Here and in the following, unless stated otherwise, q_x denotes the value of $q/10^x$ in c.g.s. units. At a radius $R > R_{dec}$ the flow decelerates assuming the Sedov-Taylor self-similar solution, so the outflow velocity can be approximated as:

$$\beta = \beta_0 \begin{cases} 1 & R \leq R_{dec} \\ (R/R_{dec})^{-3/2} & R > R_{dec} \end{cases} \quad (3)$$

If the outflow is collimated, highly relativistic and points away from a generic observer, as will typically happen

if the mergers produce short GRBs, the emission during the relativistic phase will be suppressed by relativistic beaming. Observable emission is produced only once the external shock decelerates to mildly relativistic velocities and the blast-wave becomes quasi spherical. This takes place when $\Gamma \approx 2$ namely at $R_{dec}(\beta_0 = 1)$. From this radius the hydrodynamics and the radiation become comparable to that of a spherical outflow with an initial Lorentz factor $\Gamma_0 \approx 2$. This behavior is the source of the late radio GRB orphan afterglows (Rhoads 1997; Levinson et al. 2002). Our theory is therefore applicable for the detectability of mildly and non-relativistic outflows as well as for radio orphan GRB afterglows.

Emission from Newtonian and mildly relativistic shocks is observed in radio SNe and late phases of GRB afterglows. These observations are well explained by a theoretical model involving synchrotron emission of shock accelerated electrons in an amplified magnetic field. The success of this model in explaining the detailed observations of radio Ib/c SNe (e.g., Chevalier 1998; Soderberg et al. 2005; Chevalier & Fransson 2006) allows us to employ the same microphysics here. Energy considerations show that both the electrons and the magnetic field carry significant fractions of the total internal energy of the shocked gas, $\epsilon_e \approx \epsilon_B \sim 0.1$. These values are consistent with those inferred from late radio afterglows of long GRBs (e.g., Frail et al. 2000, 2005). The observed spectra indicate that the distribution of the accelerated electrons' Lorentz factors, γ , is a power-law $dN/d\gamma \propto \gamma^{-p}$ at $\gamma > \gamma_m$ where $p \approx 2.1 - 2.5$ in mildly relativistic shocks (e.g., the radio emission from GRB associated SNe and late GRB afterglows) and $p \approx 2.5 - 3$ in Newtonian shocks (as seen in typical radio SNe; Chevalier 1998, and references therein). The value of γ_m is not observed directly but it can be calculated based on the total energy of the accelerated electrons, $\gamma_m = \frac{p-2}{p-1} \frac{m_p}{m_e} \epsilon_e \beta^2$.

The radio spectrum generated by the shock is determined by two characteristic frequencies⁵. One is

$$\nu_m \approx 1 \text{ GHz } n^{1/2} \epsilon_{B,-1}^{1/2} \epsilon_{e,-1}^2 \beta^5, \quad (4)$$

the typical synchrotron frequency of electrons with the typical (also minimal) Lorentz factor γ_m . The other is ν_a , the synchrotron self-absorption frequency. We show below that since we are interested in the maximal flux at a given observed frequency, ν_a may play a role only if it is larger than ν_m . Its value in that case is

$$\nu_a(> \nu_m) \approx 1 \text{ GHz } R_{17}^{\frac{2}{p+4}} n^{\frac{6+p}{2(p+4)}} \epsilon_{B,-1}^{\frac{2+p}{2(p+4)}} \epsilon_{e,-1}^{\frac{2(p-1)}{p+4}} \beta^{\frac{5p-2}{p+4}}. \quad (5)$$

Fig. 4 illustrates the two possible spectra, depending on the order of ν_a and ν_m . The flux at any frequency can be found using these spectra and the unabsorbed synchrotron flux at ν_m :

$$F_m \approx 0.5 \text{ mJy } R_{17}^3 n^{3/2} \epsilon_{B,-1}^{1/2} \beta d_{27}^{-2}, \quad (6)$$

where d is the distance to the source (we neglect any cosmological effects). Note that this is the real flux at ν_m only if $\nu_a < \nu_m$ (see Fig. 4).

As long as the shock is moving with a constant velocity i.e., at $t < t_{dec}$, the flux across the whole spectrum increases

⁵ The cooling frequency is irrelevant in the radio.

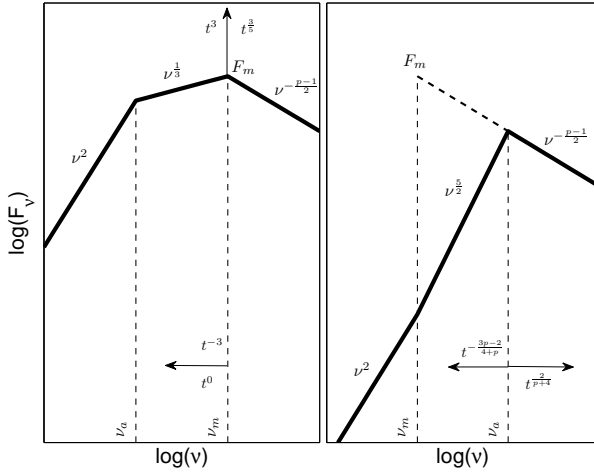


Figure 4. A sketch of the two possible spectra and the evolution of the characteristic flux, F_m , and frequencies, ν_a and ν_m . The arrows show the temporal evolution of the characteristic values. The temporal dependence before t_{dec} is noted below/to the left of the arrows while the temporal dependence after t_{dec} is noted above/to the right of the arrows. Note that the evolution of ν_m and F_m , marked only in the left spectrum, is relevant for both spectra. The evolution of ν_a , marked only in the right spectrum, is correct only when $\nu_m < \nu_a$ and is therefore relevant only in that spectrum.

(see equations 4-6). The flux evolution at later times depends on the spectrum at t_{dec} , namely on

$$\nu_{m,dec} \equiv \nu_m(t_{dec}) \approx 1 \text{ GHz } n^{1/2} \epsilon_{B,-1}^{1/2} \epsilon_{e,-1}^2 \beta_0^5, \quad (7)$$

and if $\nu_{a,dec} > \nu_{m,dec}$ then possibly on

$$\nu_{a,dec} \equiv \nu_a(t_{dec}) \approx 1 \text{ GHz } E_{49}^{2/3} n^{14/3} \epsilon_{B,-1}^{14/3} \epsilon_{e,-1}^{2/3} \beta_0^{15/3}. \quad (8)$$

The flux at that time can be found using the unabsorbed synchrotron flux at $\nu_{m,dec}$:

$$F_{m,dec} \approx 0.5 \text{ mJy } E_{49} n^{1/2} \epsilon_{B,-1}^{1/2} \beta_0^{-1} d_{27}^{-2}. \quad (9)$$

Consider now a given observed frequency ν_{obs} . We are interested in the light curve near the peak flux at this frequency. There are three possible types of light curves near the peak corresponding to: (i) $\nu_{m,dec}, \nu_{a,dec} < \nu_{obs}$, (ii) $\nu_{eq} < \nu_{obs} < \nu_{m,dec}$ and (iii) $\nu_{obs} < \nu_{eq}, \nu_{a,dec}$. Where we define

$$\nu_{eq} = 1 \text{ GHz } E_{49}^{1/7} n^{4/7} \epsilon_{B,-1}^{2/7} \epsilon_{e,-1}^{-1/7} \quad (10)$$

as the frequency at which⁶ $\nu_m = \nu_a$. In Fig. 5 we show a sketch of the time evolution of ν_a and ν_m and the corresponding ranges of ν_{obs} in which each of the cases is observed.

To estimate the time and value of the peak flux we recall, that at all frequencies the flux increases until t_{dec} . In case (i), $\nu_{m,dec}, \nu_{a,dec} < \nu_{obs}$, the deceleration time, t_{dec} ,

⁶ Note that if $\nu_{m,dec} < \nu_{a,dec}$ this equality will never take place. In that case ν_{eq} is the frequency at which this equality would have happened if Γ_0 would have been large enough (see Fig. 5)

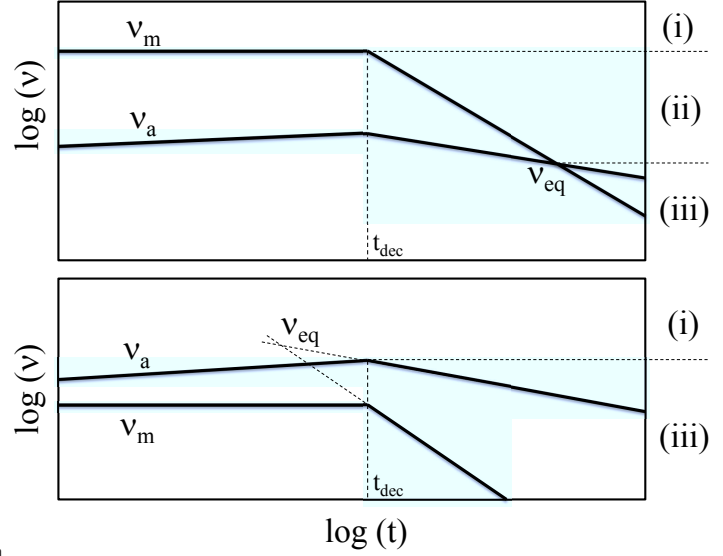


Figure 5. A sketch of the time evolution of ν_a and ν_m in two cases, $\nu_{a,dec} < \nu_{m,dec}$ (top) and $\nu_{a,dec} > \nu_{m,dec}$ (bottom). Also marked is the value of ν_{eq} . The vertical dashed line marks t_{dec} . The ranges of ν_{obs} at which each of the cases is observed is separated by horizontal dashed lines and marked on the right. Note that in the bottom panel ν_m and ν_a are not crossing each other at $t > t_{dec}$ and only two types of light curves, cases (i) and (iii), can be observed.

is also the time of the peak. The reason is that while F_m increases, ν_m decreases fast enough so that $F_{\nu_{obs}}$ decreases after t_{dec} . Note that in that case ν_a plays no role since it decreases after deceleration. Overall, in this case the flux peaks at t_{dec} and $F_{\nu_{obs},peak} = F_{m,dec} (\nu_{obs}/\nu_{m,dec})^{-(p-1)/2}$. In the two other cases, (ii) and (iii), $\nu_{obs} < \nu_{m,dec}$ and/or $\nu_{obs} < \nu_{a,dec}$ and the flux keeps rising at $t > t_{dec}$ until $\nu_{obs} = \nu_m(t)$ or $\nu_{obs} = \nu_a(t)$, whichever comes last. To find out which one of the two frequencies is it, we compare ν_{obs} with ν_{eq} . At $t > t_{dec}$, ν_m decreases faster than ν_a . Therefore in case (ii) where $\nu_{eq} < \nu_{obs}$, the last frequency to cross ν_{obs} is ν_m and the peak flux is observed when $\nu_{obs} = \nu_m(t)$. In case (iii) where $\nu_{obs} < \nu_{eq}$, the last frequency to cross ν_{obs} is ν_a and the peak flux is observed when $\nu_{obs} = \nu_a(t)$. Now, it is straight forward to calculate the peak flux, $F_{\nu_{obs},peak}$ and the time that it is observed, t_{peak} , for different frequencies. It is also straight forward to calculate the flux temporal evolution prior and after t_{dec} using equations 4-6 and the relation $t \propto R$ which holds at $t < t_{dec}$ and $\beta \propto t^{-3/5}$ at $t > t_{dec}$. The peak fluxes, the times of the peak and the temporal evolution of the three different cases are summarized in table 2. The overall different light curves are depicted in Fig. 6

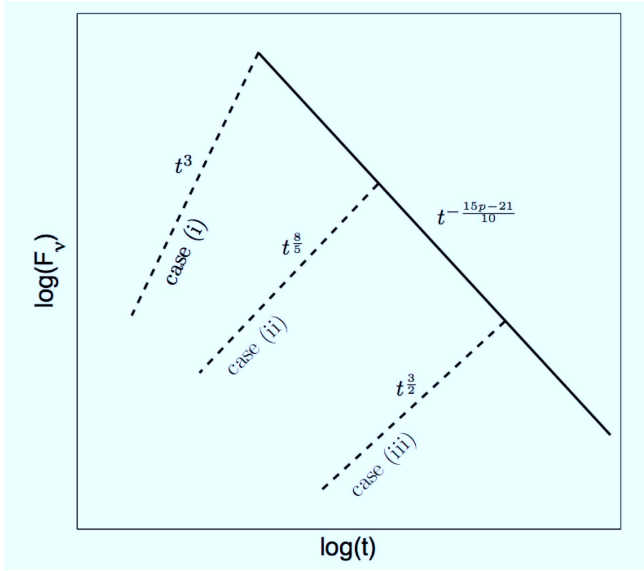
The most sensitive radio facilities are at frequencies of 1.4 GHz and higher. Equations 7 and 8 imply that in this frequency range, for most realistic scenarios, it is a case (i) light curve, i.e., $\nu_{a,dec}, \nu_{m,dec} < \nu_{obs}$. Therefore, Newtonian and mildly relativistic outflows as well as relativistic GRB orphan afterglows peak at t_{dec} with (Nakar & Piran 2011):

$$F_{\nu_{obs},peak}(\nu_{a,dec}, \nu_{m,dec} < \nu_{obs}) \approx$$

Case	$F_{\nu_{obs},peak}/F_{m,dec}$	t_{peak}/t_{dec}	$F_{\nu_{obs}}^{\dagger}$ $t < t_{peak}$	$F_{\nu_{obs}}$ $t_{peak} < t$
(i) $\nu_{m,dec}, \nu_{a,dec} < \nu_{obs}$	$(\nu_{obs}/\nu_{m,dec})^{-\frac{p-1}{2}}$	1	$\propto t^3$	$\propto t^{-\frac{15p-21}{10}}$
(ii) $\nu_{eq} < \nu_{obs} < \nu_{m,dec}$	$(\nu_{obs}/\nu_{m,dec})^{-1/5}$	$(\nu_{obs}/\nu_{m,dec})^{-1/3}$	$\propto t^{\frac{8}{5}}$	$\propto t^{-\frac{15p-21}{10}}$
(iii) $\nu_{obs} < \nu_{eq}, \nu_{a,dec}$	$\nu_{m,dec}^{\frac{p-1}{2}} \nu_{a,dec}^{-\frac{3(p+4)(5p-7)}{10(3p-2)}}$	$\nu_{obs}^{\frac{(32p-47)}{5(3p-2)}}$	$\propto t^{\frac{3}{2}}$	$\propto t^{-\frac{15p-21}{10}}$

Table 2. The observed flux before and after t_{peak} in the three different regimes.

† The temporal evolution only during the last power-law segment before t_{peak} . At earlier times the temporal evolution may be different.

**Figure 6.** Schematic light curves of the three cases. The rising phase, marked in dashed line for each of the phases, is that of the last temporal power law segment before the peak. After the peak all cases show the same power-law decay.

$$0.3 \text{ mJy } E_{49} n^{\frac{p+1}{4}} \epsilon_{B,-1}^{\frac{p+1}{4}} \epsilon_{e,-1}^{p-1} \beta_0^{\frac{5p-7}{2}} d_{27}^{-2} \left(\frac{\nu_{obs}}{1.4 \text{ GHz}} \right)^{-\frac{p-1}{2}} \quad (11)$$

The regime of $F_{\nu_{obs},peak}$ at lower radio frequencies (< 1 GHz) depends on the various parameters. If the outflow is Newtonian or the density is low or the energy is low then $\nu_{a,dec}, \nu_{m,dec} < 100$ MHz and equation 11 is applicable. Otherwise low radio frequencies are in regime (iii), i.e., $\nu_{obs} < \nu_{eq}, \nu_{a,dec}$. The flux peaks in this case at

$$t_{peak}(\nu_{obs} < \nu_{eq}, \nu_{a,dec}) \approx 200 \text{ day } E_{49}^{\frac{5}{11}} n^{\frac{7}{22}} \epsilon_{B,-1}^{\frac{9}{22}} \epsilon_{e,-1}^{\frac{6}{11}} \left(\frac{\nu_{obs}}{150 \text{ MHz}} \right)^{\frac{13}{11}}, \quad (12)$$

with

$$F_{\nu_{obs},peak}(\nu_{obs} < \nu_{eq}, \nu_{a,dec}) \approx 50 \text{ } \mu\text{Jy } E_{49}^{\frac{4}{5}} n^{\frac{1}{5}} \epsilon_{B,-1}^{\frac{1}{5}} \epsilon_{e,-1}^{\frac{3}{5}} d_{27}^{-2} \left(\frac{\nu_{obs}}{150 \text{ MHz}} \right)^{\frac{6}{5}}. \quad (13)$$

In the last two equations we used $p = 2.5$ (other p values in the range 2.1-3 yield slightly different numerical factors and power laws).

To date, the best observed signal from a mildly relativistic blast wave is the radio emission that follows GRB associated SNe. The main difference is that in these cases the circum burst medium is typically a wind (i.e., $n \propto R^{-2}$) and therefore the density at early times is much larger than in the ISM and self absorption plays the main role in determining the light curve. A good example for comparison of equation 11 with observations is the light curve of SN 1998bw. This light curve is observed at several frequencies at many epochs, enabling a detailed modeling that results in tight constraints of the blast wave and microphysical parameters. Li & Chevalier (1999) find that at the time of the peak at 1.4 GHz, about 40 days after the SN, taking $\epsilon_e = \epsilon_B = 0.1$, the energy in the blast wave is $\sim 10^{49}$ erg, its Lorentz factor is ~ 2 and the external density at the shock radius is $n \sim 1 \text{ cm}^{-3}$. The peak is observed when $\nu_m, \nu_a \leq \nu_{obs}$ and it depends only on these parameters (it is only weakly sensitive to the density profile). Therefore, equation 11 is applicable in that case. Indeed, plugging these numbers into equation 11 we obtain a flux of 20 mJy at the distance of SN 1998bw (40 Mpc), compared to the observed flux of 30 mJy. This is not surprising given that the model we use is based on that of radio SNe.

3.2 An outflow with a power-law velocity profile

The numerical simulations provide profiles of the outflow energy as a function of the velocity. Similarly to the case of an outflow with a single velocity we approximate the blast wave to be spherical. The main difference when a range of velocities is considered, is that in addition to the forward shock, which is driven into the circum burst medium, there is a continuous reverse shock that is driven into the ejecta. If most of the outflow energy resides in low velocities then this reverse shock drives an increasing amount of energy into the shocked region, mitigating the deceleration of the forward shock. In that case the mass collected by the forward shock, $M(R)$, when its velocity is β and its radius is R , is comparable to the mass in the ejecta with velocity $\geq \beta$. Thus the relation between the radius and the velocity can be found at any time by equating:

$$M(R)(\beta c)^2 = E(\geq \beta), \quad (14)$$

where this equality is correct up to a factor of order unity that depends on the exact ejecta profile. Chevalier (1982) calculates self-similar solutions for an outflow with a power-law distribution $\rho \propto \beta^{-k}$ in which most of the energy is at low velocities, i.e., for $k > 5$ since $E(> \beta) \propto \beta^{-(k-5)}$.

Chevalier (1982) provides the exact coefficients of the solution for several values of k , all providing corrections of order unity to equation 14.

In §3.3 we apply equation 14 to the results of the numerical simulations and we calculate the resulting light curves from the ejecta profiles. However before doing so, we use equation 14 to find $R(t)$ and $\beta(t)$ for an outflow with a power-law velocity profile and we find an analytic solution for the flux for a power-law velocity profile. Consider an outflow with a power-law velocity profile and a minimal velocity β_{\min} and a total energy $E(> \beta_{\min}) = E_{\text{tot}}$, that propagates in a constant density medium. Equation 14 implies that its radius and velocity evolve with time as:

$$R = \left(\frac{3k^{k-3}(\beta_{\min}c)^{k-5}E_{\text{tot}}}{4\pi(k-3)^{k-3}nm_p} \right)^{\frac{1}{k}} t^{\frac{k-3}{k}} \\ \approx 4 \cdot 10^{17} \left(\frac{E_{\text{tot},50}}{n} \right)^{\frac{1}{k}} \left(\frac{\beta_{\min}}{0.2} \right)^{\frac{k-5}{k}} t_{\text{year}}^{\frac{k-3}{k}} \text{ cm} \quad (15)$$

$$\beta = \left(\frac{3(k-3)^3(\beta_{\min}c)^{k-5}E_{\text{tot}}}{4\pi k^3 nm_p} \right)^{\frac{1}{k}} t^{-\frac{3}{k}} \\ \approx 0.3 \left(\frac{E_{\text{tot},50}}{n} \right)^{\frac{1}{k}} \left(\frac{\beta_{\min}}{0.2} \right)^{\frac{k-5}{k}} t_{\text{year}}^{-\frac{3}{k}} \quad (16)$$

plugging these values into equations 4-6 we find that for relevant parameters $\nu_a, \nu_m < 1.4$ GHz and

$$F_\nu(\nu > \nu_a, \nu_m) \approx 50 \mu\text{Jy} e^{-3.4(p-2.5)} E_{\text{tot},50}^{\frac{3+5p}{2k}} \left(\frac{\beta_{\min}}{0.2} \right)^{\frac{(3+5p)(k-5)}{k}} \\ n^{\frac{5k-10p+k-6}{k}} \epsilon_{B,-1}^{\frac{p+1}{4}} \epsilon_{e,-1}^{p-1} d_{27}^{-2} t_{\text{year}}^{\frac{3(2k-3-5p)}{2k}} \\ = 50 \mu\text{Jy} E_{\text{tot},50}^{0.86} \left(\frac{\beta_{\min}}{0.2} \right)^{3.44} n \epsilon_{B,-1}^{7/8} \epsilon_{e,-1}^{3/2} d_{27}^{-2} t_{\text{year}}^{5/12} \\ (k=9; p=2.5). \quad (17)$$

This equation is applicable starting at t_{dec} that corresponds to the maximal velocity⁷, β_{max} , and the energy that is carried by the material that moves at the maximal velocity (i.e., $E_{\beta_{\text{max}}} \approx E_{\text{tot}}(\beta_{\text{max}}/\beta_{\min})^{-k+5}$) and up to t_{dec} that corresponds to β_{\min} and E_{tot} . At earlier times then $t_{\text{dec}}(\beta_{\text{max}}, E_{\beta_{\text{max}}})$ the light curve is the one described in table 2 (with β_{max} and $E_{\beta_{\text{max}}}$) and at later times then $t_{\text{dec}}(\beta_{\min}, E_{\text{tot}})$ it joins the decaying light curve described in table 2 ($F_\nu \propto t^{(21-15p)/10}$).

3.3 Radio Light curves from the simulated outflows

To calculate the electromagnetic signatures we use the ejecta velocity profiles from the simulations and apply the approximations of §3.2. We use equation 14 to find $R(t)$ and $\beta(t)$ and subsequently plug them into equations 4-6 to calculate the light curve. We approximate the ejecta-ambient medium interaction as a spherical blast wave that propagates into a constant density, n . Behind the shock constant fractions of the internal energy, $\epsilon_e = 0.1$ and $\epsilon_B = 0.1$, are deposited in relativistic electrons and in magnetic field, where the electrons are accelerated to a power-law with an index $p = 2.5$.

⁷ We assume that the maximal velocity ejecta is still mildly relativistic, i.e., $\gamma_{\text{max}}\beta_{\text{max}} \lesssim 1$.

Inspection of the various ns² merger simulations reveal relatively large kinetic energies (at least 10^{50} erg and at times near 10^{51} erg, see Tab. 1) but with relatively low average velocities, around $0.1c - 0.16c$. The corresponding peak fluxes and durations correspond, therefore, to the sub-relativistic case examined in Nakar & Piran (2011). We calculate, for these simulated mergers, the light curves at two frequencies, 1.4 GHz and 150 MHz, and for two values of external densities $n = 1 \text{ cm}^{-3}$ and $n = 0.1 \text{ cm}^{-3}$. The flux normalization is for events at a distance of 10^{27} cm, roughly at the detection horizon for ns² mergers by advanced LIGO and Virgo.

Here we calculate the radio emission only from the dynamical component of the ejecta (see section 2). This component is launched preferentially along the equatorial plane, while faster moving outflows (related to processes a and c discussed in section 2) are launched along the rotation axis. As a result the fast moving ejecta can propagate to large distances, ahead of the dynamical ejecta, and interact with the ambient medium. The faster moving components are expected to carry less energy than the slow moving ejecta. Yet, the strong dependence of the radio peak flux on the outflow velocity (equation 11) and the short deceleration time of the fast moving ejecta (weeks to months) imply that it is expected to dominate radio emission before the dynamical ejecta start decelerating (months-years). Thus, our estimates in this section are only lower limits on the true radio emission at early time (up to about a year for $n = 1 \text{ cm}^{-3}$ and about three years for $n = 0.1 \text{ cm}^{-3}$). A glimpse of the influence of a mildly relativistic material can be seen in Figs. 11 and 12 below which depicts the light curves of nsbh mergers. Our simulations find that a mildly relativistic material is ejected in the $1.4 m_\odot$ ns - $5 m_\odot$ bh case. Although it carries a much lower energy than the slower moving ejecta its strong effect is seen a early times. Since we expect the dynamical ejecta to be the most massive and most energetic of all the outflow components, it is not expected to be affected significantly by possible interaction between the different outflow components. If this is the case then our radio predictions are good approximations to the true emission at later times. If however, the fast outflow is more energetic than the slow one, then also our late time radio estimates are only lower limits of the true emission.

The resulting light curves are shown in Figs. 7-12. Figs. 7 and 8 depict the radio light curves of the various ns² mergers for $n = 1 \text{ cm}^{-3}$. Our canonical case, a merger of two $1.4 m_\odot$ neutron stars is marked in both figures with a thick solid line. The flux of the canonical merger is 0.04 mJy (0.2 mJy) at 1.4 GHz (150 MHz) 1-4 years after the merger. It shows almost minimal emission among all equal mass mergers (Fig. 7), the emission increases by a factor of 5 (at 1.4 GHz) for a $1.8-1.8 m_\odot$ pair and it is almost similar for $1.0-1.0 m_\odot$. Fig. 8 depicts mergers with combinations of different ns masses. In mergers with a larger mass difference the secondary is disrupted more completely, producing a more prominent tidal tail. Therefore, the ejected mass rises with the mass ratio (see Tab. 1 and Fig. 1). As a result, the dynamically ejected outflows from unequal mass mergers, produce in general brighter and longer lived radio remnants. Indeed, in most cases of unequal mass mergers the luminosities, both in the 1.4 GHz and at 150 MHz , are brighter at late times than the equal mass case. In some cases they reach 0.3 mJy (2 mJy)

Table 3. Basic properties of Radio Flares from the sub-relativistic dynamically ejected outflow for selected cases

Run	Masses m_\odot	$n = 1\text{cm}^{-3}$				$n = 0.1\text{cm}^{-3}$			
		1.4 GHz		150 MHz		1.4 GHz		150 MHz	
		$F_\nu(\text{peak}^a)$ mJy	$t(\text{peak}^a)$ yr	$F_\nu(\text{peak}^a)$ mJy	$t(\text{peak}^a)$ yr	$F_\nu(\text{peak}^a)$ μJy	$t(\text{peak}^a)$ yr	$F_\nu(\text{peak}^a)$ μJy	$t(\text{peak}^a)$ yr
8	1.4 -1.2	0.09	4	0.5	4	10	9	50	9
12 ^b	1.4 -1.4	0.04	1.5	0.2	2	5	3	30	3
15 ^c	1.4 - 2.0	0.3	5	2	6	50	10	200	10
23 ^d	1.4 - 10	1.5	4	4	8	200	10	1000	10

^a This is the peak of the sub-relativistic outflow. A mildly relativistic outflow, not calculated here, may produce a stronger and earlier peak.

^b The canonical ns^2 case.

^c This is the maximal signal from our runs of ns^2 mergers

^d nsbh merger.

a few years after the merger. Note that even a small mass difference of less than 15% can make a large difference in the observed luminosity. For example, a 1.4-1.2 m_\odot merger produces twice as bright and twice as long remnant compared to a 1.4-1.4 m_\odot merger.

The external density is a critical parameter. Figs. 9 and 10 depict the resulting light curves when the density is $n = 0.1 \text{ cm}^{-3}$ for $t > 3 \text{ yr}$. In that case the signal, at the two considered frequencies, is almost an order of magnitude fainter in all cases, compared with $n = 1 \text{ cm}^{-3}$. At 1.4 GHz the signal also evolves slower. Since the self absorption frequency is below 150 MHz in that case, the light curves at both 1.4 GHz and 150 MHz have quite similar shapes.

Mergers of a black hole and a neutron star eject even larger amounts of mass. Their signals, shown in Figs. 11 and 12, are stronger reaching 1 mJy at 1.4 GHz and a few mJy at 150 MHz. The time scales are also longer and reach a few years at densities of 1 cm^{-3} and about 10 year at 0.1 cm^{-3} .

4 DETECTION AND IDENTIFICATION

4.1 Detectability

We use the radio light curves of our canonical ns^2 merger (1.4-1.4 m_\odot) to estimate their detectability by current and future radio facilities. The estimates based on this merger case are conservative. First, since other merger cases, and especially those with even a minor mass difference between the coalescing stars, are brighter and second since our simulations do not include all outflow sources. We also consider here the detectability of nsbh merger based on the light curves calculated for a 1.4-10 m_\odot merger. Table 4 shows the detection horizons for these two merger scenarios for different radio telescopes and two external densities ($n = 1\text{cm}^{-3}$ and $n = 0.1\text{cm}^{-3}$).

The radio flares depend sensitively on the surrounding circum-merger density. Current robust knowledge concerning ns^2 binaries arises from the observed Galactic population. These binaries are all observed in the Galactic disk whose typical density is about 1 cm^{-3} Draine (2011). Hence we expect that this is the most relevant density to consider. In particular we stress that the estimated rate of ns^2 , that are based on these binaries (and used later when we estimate the detection rate of these radio flares) are all relevant

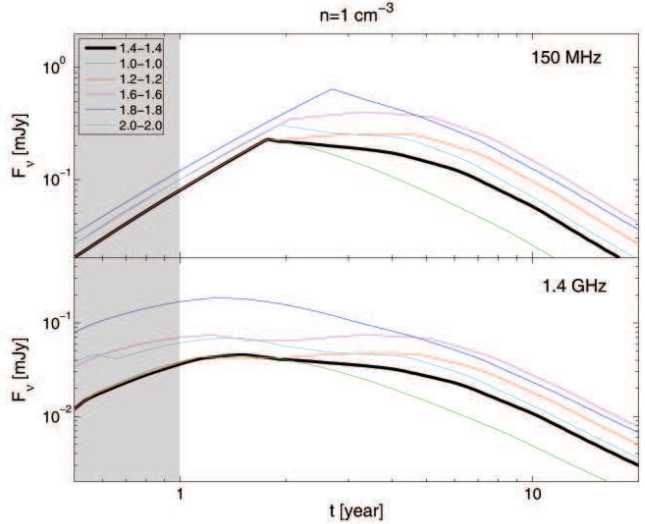


Figure 7. Radio light curves generated by interaction of the dynamically ejected sub-relativistic outflows from equal mass ns^2 mergers at 150 MHz and 1.4 GHz for 1 cm^{-3} circum-merger density, $\epsilon_B = \epsilon_e = 0.1$ and $p = 2.5$. The merger distance is 10^{27} cm , roughly the detection horizon for ns^2 mergers by advanced LIGO and Virgo. The shaded region at $t < 1 \text{ yr}$ reflect the fact that at this time the emission is expected to be dominated by mildly relativistic outflows, which are not included in our simulations.

for this particular population. An additional hypothetical population of ns^2 mergers that take place in a much lower density environment and might produce weaker signals is not included in our radio counterpart estimates.

A ns^2 merger that takes place in $n = 1\text{cm}^{-3}$ environment produces a radio remnant that can be easily observed by EVLA (1 hour integration) all the way to the advanced LIGO/Virgo detection horizon, with a rise time of $\sim 1 \text{ yr}$ and a decay time of several years. However, given the relative narrow EVLA field of view it requires either a $\sim \text{deg}^2$ localization or a dedicated search in a larger error box. Given that the planned localization of advanced GW detectors is $\sim 10 - 100 \text{ deg}^2$ for events with a detector network signal to noise ratio of 10 (Wen & Chen 2010), a targeted search in the error box of a GW signal is certainly feasible. For that purpose other facilities, with lower sensitivity but sig-

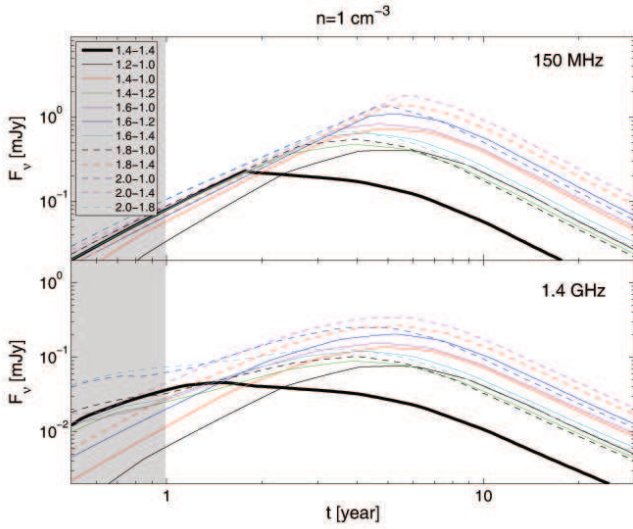


Figure 8. Same as Fig. 7 for different combinations of binary ns masses.

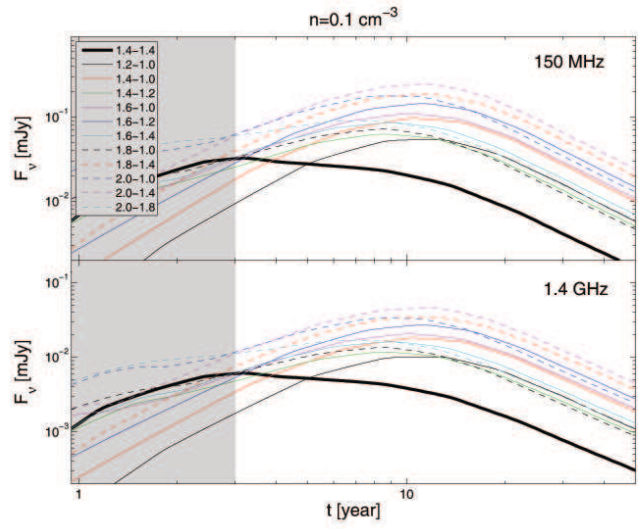


Figure 10. Same as Fig. 9 for different combinations of binary ns masses.

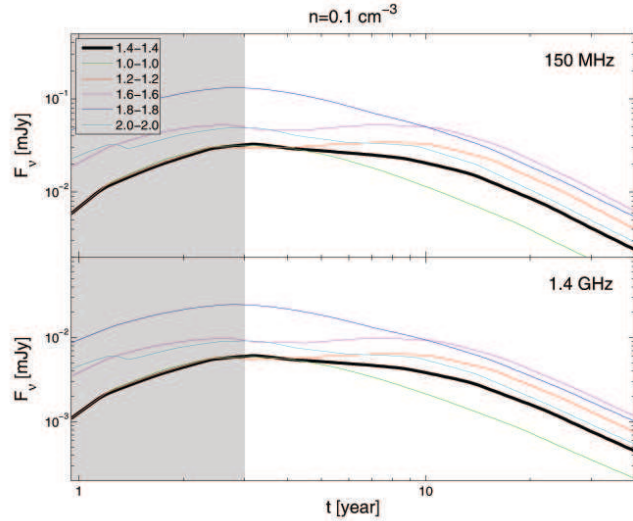


Figure 9. Same as Fig. 7 for a equal mass mergers and density of $n = 0.1\text{cm}^{-3}$. With the lower external density the effect of mildly relativistic outflows extends now up to about 3 years and hence the shaded region is larger.

nificantly larger field-of-view (e.g., ASKAP) may be more appropriate.

A ns^2 merger in $n = 0.1\text{cm}^{-3}$ environment requires a more dedicated effort (10 hours) in order to detect the resulting signal out to 300 Mpc by the EVLA. The rise and decay time are significantly longer (years and a decade respectively). This makes the search for ns^2 transients, even in the case of a $\sim 10\text{--}100\text{ deg}^2$ GW localization, very challenging, unless they produce at least 10^{49} erg in mildly relativistic outflow (which is not accounted for by our simulations).

nsbh mergers produce significantly brighter signals, and are therefore detectable up to a greater distances, $\gtrsim 1$ Gpc, by the EVLA and near future facilities, even for density of $n = 0.1\text{cm}^{-3}$. This distance is similar to the detection horizon of these events by the advanced GW detectors. This

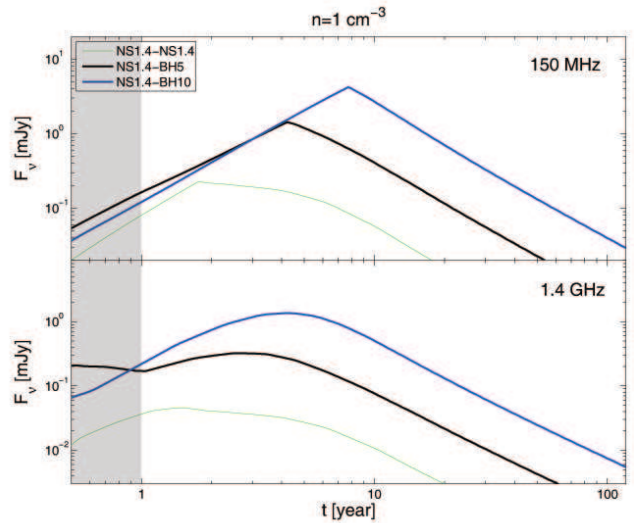


Figure 11. Light curves for nsbh mergers of various masses. Parameters are the same as Fig. 7. For comparison the result of the standard ns^2 merger case is shown as a thin line. The strong effect of a modest mildly relativistic ejecta at early time can be seen in the $1.4m_\odot$ ns- $5m_\odot$ bh case in the 1.4 GHz lightcurve.

makes nsbh mergers a promising target, however, the observed rate depends of course on their unknown merger rate.

Next we consider detectability in a blind radio survey. The number of radio remnants in a single snapshot all sky radio image is $N_{\text{all-sky}} = \mathcal{R}V\Delta t$, where V is the detectable volume, Δt is the time that the flux is above the detection limit and \mathcal{R} is the event rate. Assuming a single velocity outflow with typical parameters the 1.4 GHz light curve is a case (i) (see §3). Thus, we use equations 2 and 11, and the approximation $\Delta t \approx t_{\text{dec}}$, to find that the number of radio coalescence remnants in a single 1.4 GHz whole sky snapshot with a detection limit \mathcal{F} (see also supplementary material in Nakar & Piran (2011):

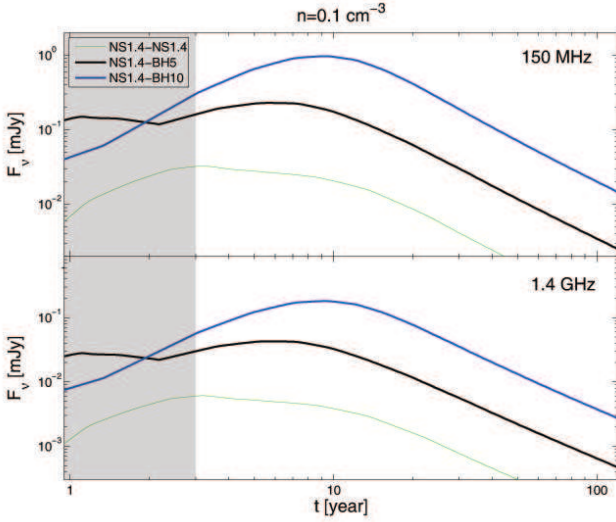


Figure 12. Light curves for nsbh mergers of various masses. Parameters are the same as Fig. 7 but the density is 0.1 cm^{-3} . The strong effect of a modest mildly relativistic ejecta at early time can be seen in the $1.4 m_\odot$ ns- $5 m_\odot$ bh case in both 150 MHz and 1.4 GHz lightcurves.

$$N_{all-sky}^{1.4\text{GHz}} \approx 20 E_{49}^{11/6} n^{\frac{9p+1}{24}} \epsilon_{B,-1}^{\frac{3(p+1)}{8}} \epsilon_{e,-1}^{\frac{3(p-1)}{2}} \beta_0^{\frac{45p-83}{12}} \mathcal{R}_{300} \mathcal{F}_{-1}^{-3/2}. \quad (18)$$

Where $\mathcal{F}_{-1} = \mathcal{F}_{lim}/0.1 \text{ mJy}$ and \mathcal{R}_{300} is the merger rate in units of $300 \text{ Gpc}^{-3} \text{ yr}^{-1}$. Plugging values from Table 1 for the different runs we can obtain a first estimate, including the dependence on the circum merger density and micro-physical parameters, of the number of all sky flares that are detectable. A better estimate for specific parameters can be obtained using the light curves we calculated in §3.3. Again we take $1.4-1.4 m_\odot$ as the canonical ns² merger and $1.4-10 m_\odot$ as the canonical nsbh merger.

A $1.4-1.4 m_\odot$ ns² merger that takes place in $n = 1 \text{ cm}^{-3}$ environment is brighter than 0.1 mJy at 1.4 GHz for about 4 years at a distance of 150 Mpc . Therefore, if as suggested by Galactic ns², this is the density of a typical merger environment, then $N_{all-sky}^{ns^2} \sim 20 \mathcal{R}_{300}^{ns^2} \mathcal{F}_{-1}^{-3/2}$. If however, typical ns² merger takes place at $n = 0.1 \text{ cm}^{-3}$ environment the number of remnants in an all sky snapshot drops by an order of magnitude.

A $1.4-10 m_\odot$ nsbh merger that takes place in $n = 1 \text{ cm}^{-3}$ environment is brighter than 0.1 mJy at 1.4 GHz for about 4 years at a distance of 1 Gpc , implying $N_{all-sky}^{nsbh} \sim 20 \mathcal{R}_{300}^{nsbh} \mathcal{F}_{-1}^{-3/2}$, where \mathcal{R}_{300}^{nsbh} is the nsbh merger rate in units of $\text{Gpc}^{-3} \text{ yr}^{-1}$. Again, if the typical nsbh circum-merger density is $n = 0.1 \text{ cm}^{-3}$ then $N_{all-sky}$ drops by an order of magnitude.

To conclude, our calculations here strengthen the results of Nakar & Piran (2011) that there is a fair chance to detect merger radio remnants in a sub-mJy survey of even a part of the sky and a high chance to detect them in a whole sky survey. Such survey's of a small portion of the sky are planned already with the EVLA, while a sub-mJy large scale transient survey is part of the ASKAP Survey Science Projects⁸. Finally, a 1 mJy 150 MHz survey with LOFAR will

find a comparable number of remnants, but these will have a longer rise time, and therefore will be harder to identify.

4.2 A comparison with short GRBs' radio orphan afterglows

The outflows of short GRBs begin highly relativistic and probably highly beamed. Eventually they slow down and become detectable from all directions (see §3). Therefore, the rate estimate equation 18 is also applicable for radio orphan afterglows when $\beta_0 = 1$. However some of the parameters in equation 18 are not directly observable. The observed quantities are the isotropic equivalent γ -ray energy, $E_{\gamma,iso}$, and the rate of bursts that point to the observer \mathcal{R}_{obs}^{SHB} , while equation 18 depends on $E = E_{iso} f_b$ and $\mathcal{R}^{SHB} = \mathcal{R}_{obs}^{SHB} f_b^{-1}$, where $f_b < 1$ is the fraction of the 4π steradian covered by the jet and E_{iso} is the isotropic equivalent energy in the afterglow blast wave. X-ray observations indicate that γ -ray emission in short GRBs is very efficient and that in general $E_{iso} \sim E_{\gamma,iso}$ (Nakar 2007). In the following discussion we assume that this is the case.

$E_{\gamma,iso}$ of short GRBs ranges at least over four orders of magnitude ($10^{49} - 10^{53} \text{ erg}$). The rate of observed short GRBs is dominated by 10^{49} erg bursts, and the luminosity function can be well approximated by a power-law, at least in the range $\sim 10^{49} - 10^{51} \text{ erg}$, such that $\mathcal{R}_{obs}^{SHB}(E) \sim 10 E_{iso,49}^{-\alpha} \text{ Gpc}^{-3} \text{ yr}^{-1}$ where $\alpha \approx 0.5 - 1$ (Nakar et al. 2006; Guetta & Piran 2006). Plugging these into equation 18 we obtain

$$N_{all-sky}^{1.4\text{GHz}}_{SHB} \approx 1 f_b^{5/6} E_{iso,49}^{\frac{11}{6}-\alpha} n^{\frac{9p+1}{24}} \epsilon_{B,-1}^{\frac{3(p+1)}{8}} \epsilon_{e,-1}^{\frac{3(p-1)}{2}} \mathcal{F}_{lim,-1}^{-3/2}. \quad (19)$$

This equation is similar to equation 9 of Levinson et al. (2002), with the observed luminosity function already folded in.

Narrower beamed bursts (with lower f_b) are more numerous and they produce less total energy per burst. The positive dependence of equation 19 on f_b implies that overall the lower energy is “winning” over the increased rate, and the detectability of narrower bursts is lower. Using, equation 19 we can put a robust upper-limit on the orphans rate since all the parameters are rather well constrained by observations, with the exception of f_b which is < 1 by definition. Therefore, assuming that short GRBs are beamed, the detection of the common $\sim 10^{49} \text{ erg}$ bursts in a blind survey, even with next generation radio facilities, is unlikely (Nakar 2007). However, brighter events should be detectable. If the beaming is energy independent, detectability increases with the burst energy. The luminosity function possibly breaks around 10^{51} erg , in which case the orphans number is dominated by 10^{51} erg bursts. For $f_b^{-1} = 30$ we expect from these bursts ~ 10 orphan afterglows brighter than 0.1 mJy at a single 1.4 GHz whole sky snapshot.

So far we discussed detectability in a blind survey. A followup dedicated search would be, of course, more sensitive. If compact binary mergers produce short GRBs then the energy of most GW detected bursts will be faint with $E_{\gamma,iso} \sim 10^{49} \text{ erg}$. The chance to detect their orphan afterglows again depended on their total energy and thus on f_b . Equation 11 shows that if $f_b^{-1} = 30$ then detection should be difficult but possible in a dedicated search mode. Note that since the energy of the burst is low, the radio emission will

⁸ <http://www.atnf.csiro.au/projects/askap/ssps.html>

Table 4. Properties and detection horizons (neglecting cosmological corrections) of the sub-relativistic dynamically ejected outflow from 1.4-1.4 m_{\odot} ns^2 and 1.4-10 m_{\odot} $nsbh$ mergers with different radio facilities.

Radio Facility	Obs Freq. (GHz)	Field of view (deg ²)	1 hr rms μ Jy	ns^2 1 hr horizon [†] $n = 1cm^{-3}$	ns^2 10 hr horizon ^{††} $n = 0.1cm^{-3}$	$nsbh$ 1 hr horizon [†] $n = 1cm^{-3}$	$nsbh$ 10 hr horizon ^{††} $n = 0.1cm^{-3}$
EVLA ^a	1.4	0.25	7	360 Mpc	200Mpc	1.8 Gpc	1.4 Gpc
ASKAP ^b	1.4	30	30	170 Mpc	100 Mpc	850Mpc	700 Mpc
MeerKAT ^c	1.4	1.5	35	160 Mpc	90 Mpc	800 Mpc	650 Mpc
Apertif ^d	1.4	8	50	135 Mpc	75 Mpc	670 Mpc	550 Mpc
LOFAR ^e	0.15	20	1000	70 Mpc	40 Mpc	300Mpc	250 Mpc

[†] The distance at which the observed peak flux is 4 times the 1 hr rms.

^{††} The distance at which the observed peak flux is 4 times the 10 hr rms.

^a <http://www.aoc.nrao.edu/evla/>

^b <http://www.astron.nl/general/apertif/apertif>

^c <http://www.atnf.csiro.au/projects/askap/technology.html>

^d <http://www.ska.ac.za/meerkat/>

^e <http://lofar.org>

evolve quickly, reaching a peak and decaying on a week time scale, so a prompt and rather deep search will be needed.

4.3 Identification and contamination

A key issue with the detection of compact binary merger remnants in blind surveys is their identification. Ofek et al. (2011) and Frail et al. (2012) present a census of the transient radio sky. Luckily the transient radio sky at 1.4 GHz is relatively quiet. The main contamination source are radio active Galactic nuclei (AGNs), however their persistent emission is typically detectable in other wavelength and/or deeper radio observations. Moreover, the signal from a compact binary merger is expected to be located within its host galaxy (otherwise the density is too low), but away from its center. The host and the burst location within it, should be easily detectable at the relevant distances.

The only known, and guaranteed, transient 1.4 GHz source with similar properties are radio SNe. Among these typical radio SNe are the most abundant. A transient search over 1/17 of the sky with $F_{lim} = 6$ mJy at 1.4GHz (Levinson et al. 2002; Gal-Yam et al. 2006; Ofek et al. 2010) finds one radio SN. This rate translates to $10^3 - 10^4$ SNe in a whole sky $F_{lim} = 0.1$ mJy survey. These contaminants can be filtered in three ways. First, by detection of the SN optical light. However, the optical signal may be missed if it is heavily extinguished, and given the large number of radio SNe, misidentifying even a small fraction of them may render the survey useless for our purpose. The second filter is the optically thick spectrum at high radio frequency (~ 10 GHz) at early times, which is a result of the blast wave propagation in a wind. Thus, a multi-wavelength radio survey can identify radio SNe. The last filter is the luminosity-time scale relation of typical radio SNe that is induced by the outflow velocity (e.g., Fig. 2 in Chevalier et al. 2006). Type II SN outflows are slow, $\sim 0.01c$, and therefore their radio emission is longer/fainter than that expected for merger remnants. The common type of Ib/c radio SNe is produced by $\sim 0.2c$ blast waves but with much less energy than what we expect from a binary merger outflow, and therefore their radio emission is much fainter. The combination of any two

of these filters will hopefully be enough to identify all the typical radio SNe.

Slightly different contaminants are GRBs associated SNe. Their outflows are as fast and as energetic as those that we expect from a binary merger and therefore their radio signature is similar in time scales and luminosities. SN1998bw-like events are detectable by a 0.1 mJy survey at 1.4 GHz up to a distance of several hundred Mpc for 40 days and their rate is $40 - 700$ Gpc⁻³ yr⁻¹ (Soderberg et al. 2006), implying at least several sources at any whole sky snapshot. Here only the first filter (SN optical light) and possibly the second (optically thick spectrum) can be applied. However, given the high optical luminosity of GRBs associated SNe and their relatively low number this should be enough in order to filter them out. These contaminants highlight the importance of a multi-wave length strategy where an optical survey accompanies the radio survey to best utilize both surveys' detections.

Finally, radio is the place to look for blast waves in tenuous mediums, regardless of their origin. Any source of such an explosion, be it a binary merger, a GRB or a SN, produces a radio signature. Therefore, all the strong explosions may be detectable in a deep radio survey, this includes for example long GRB on-axis and off-axis afterglows and giant flares from extragalactic soft gamma-repeaters. The difference between the radio signatures of the different sources (amplitude, spectrum and time evolution) depends on the blast wave energy and velocity and on the external medium properties. We thus will be able to identify the characteristics of binary mergers outflows. If, however, there is a different source of $\sim 10^{50}$ erg of sub- or mildly relativistic outflow that explodes in the ISM it will be indistinguishable from binary mergers (at least in the radio). Currently we are not aware of any such source, with the exception of long GRBs at the low end of the luminosity function, but these are too rare to contaminate a survey. Any other source of such outflows, if existent, will probably be a part of the family of collapsing/coalescing compact objects.

5 IR-UV TRANSIENTS FROM RADIOACTIVE DECAYS, “MACRONOVAE”

The ejected material is extremely neutron rich and rapidly expanding. Under such conditions rapid neutron capture is hard to avoid (Hoffman et al. 1996; Freiburghaus et al. 1999; Roberts et al. 2011; Korobkin et al. 2012). The latter study finds that ns^2 and nsbh mergers produce a unique, solar-system-like r-process abundance pattern for nucleon numbers $A > 120$, independent of the astrophysical parameters of the merging binary system. The r-process itself occurs on a very short time scale, but the freshly synthesized elements subsequently undergo nuclear fission, alpha- and beta-decay which occur on much longer time scales. The supernova-like emission from this expanding material was first suggested by Li & Paczyński (1998) and discussed later by Kulkarni (2005) and Metzger et al. (2010). We combine the ejecta velocity profiles found in our simulations with the time dependent radioactive power injection found in the recent r-process study of Korobkin et al. (2012) to calculate bolometric light curves.

The optical depth of the expanding outflow decreases with time, and as a result larger amounts of mass become visible to the observer. The ejected mass has a gradient of velocities. We denote as $m(v)$ the mass with asymptotic velocity at infinity $> v$. Before the peak of the emission, the observed mass, m_{obs} , is the one for which the diffusion time is comparable to the expansion time, namely $\tau_{\text{obs}} \approx c/v$, where $\tau(m) \approx \kappa m / (4\pi v^2 t^2)$ (note that $m = m(v)$) and κ is the opacity cross-section per unit of mass. The emission peaks at t_{peak} , when the entire ejecta become observable, namely at the first time that $m_{\text{obs}} = m_{\text{ej}}$. At later time the entire ejecta are exposed and $m_{\text{obs}}(t > t_{\text{peak}}) = m_{\text{ej}}$.

A major uncertainty in the light curve calculation is the opacity of r-process elements. The opacity determines first the bolometric luminosity and second its spectrum. Here we assume a constant and grey opacity in order to determine the luminosity, which is less sensitive to the detailed wavelength dependence of the opacity. We do not attempt to predict the observed spectrum. Metzger et al. (2010) discussed the opacity of the neutron rich ejecta expect it to be similar to that of iron-group elements, which they approximate as a constant $\kappa = 0.1 \text{ cm}^2/\text{g}$. Below we use it as the canonical value.

At any time prior to t_{peak} the observed mass is

$$m_{\text{obs}}(t < t_{\text{peak}}) \approx 0.05 M_{\odot} \left(\frac{\kappa}{0.1 \text{ cm}^2/\text{g}} \right)^{-1} \left(\frac{t}{\text{day}} \right)^2 \left(\frac{v}{0.1c} \right). \quad (20)$$

Note that this is an implicit equation since v itself depends on m_{obs} . Thus, m_{obs} increases with time (slightly slower than t^2 , since v decreases with m) until all of the ejecta is exposed at t_{peak} . The observed luminosity is dominated by the energy release via radioactive decay. Korobkin et al. (2012) follow the nucleosynthesis of a number of fluid elements that are ejected at different velocities and during different stages of the merger and find that all of them result in a similar radioactive energy injection rate per unit of mass into the expanding ejecta that can be approximated by

$$\dot{\epsilon} = 2 \cdot 10^{18} \left[\frac{1}{2} - \frac{1}{\pi} \arctan \left(\frac{t - t_0}{\sigma} \right) \right]^{1.3} \times \frac{\epsilon_{\text{therm}}}{0.5} \text{ erg/g/s} \quad (21)$$

where $t_0 = 1.3 \text{ s}$ and $\sigma = 0.11 \text{ s}$ and ϵ_{therm} is the fraction of injected energy that is emitted as thermalized radiation and

Table 5. Basic properties of Macronovae for selected cases

Run	Masses m_{\odot}	m_{ej} $10^{-2} m_{\odot}$	$L(\text{peak})^{\dagger}$ 10^{41} erg/s	$t(\text{peak})$ day	magnitude ‡ at 300 Mpc
8	1.4 - 1.2	2.1	6 [1.5]	0.4 [1.5]	22 [24]
12 ^a	1.4 - 1.4	1.3	5 [1]	0.4 [1.5]	22 [24]
15 ^b	1.4 - 2.0	3.9	9 [2]	0.6 [2]	21.5 [23.5]
23 ^c	1.4 - 10	4.9	11 [2.5]	0.6 [2]	21 [23]

All values are assuming $\kappa = 0.1 \text{ cm}^2/\text{g}$ [$\kappa = 1 \text{ cm}^2/\text{g}$]

† Bolometric thermalized luminosity/magnitude, emitted mostly in IR, optical and

^a The canonical ns^2 case.

^b This is the maximal signal among the ns^2 mergers runs.

^c nsbh merger.

not as unobserved neutrinos or gamma-rays. The value of ϵ_{therm} is not well constrained and below we use the default value of Korobkin et al. (2012), $\epsilon_{\text{therm}} = 0.5$. On the relevant time scales equation 21 corresponds to the Li & Paczyński (1998) coefficient $f = 10^{-6} (t/\text{day})^{-0.3}$. The resulting bolometric (thermalized) luminosity is:

$$L \sim m\dot{\epsilon} \sim 2 \times 10^{41} \text{ erg s}^{-1} \frac{\epsilon_{\text{therm}}}{0.5} \left(\frac{m_{\text{obs}}}{10^{-2} M_{\odot}} \right) \left(\frac{t}{\text{day}} \right)^{-1.3}. \quad (22)$$

Note that at early times L increases because m_{obs} increases almost like t^2 . This luminosity is emitted in the IR to UV range. At early time L is increasing (slightly slower than linearly). The luminosity peaks when the entire ejecta is seen (roughly at $t = 0.5 \text{ day}$), and the light curve decays afterwards roughly as $t^{-1.3}$. The value of m_{obs} is inversely proportional to the opacity. Therefore higher opacity implies a slower evolving and dimmer signal, and it most likely results in a redder transient.

The resulting macronova light curves, assuming $\kappa = 0.1 \text{ cm}^2/\text{g}$, are shown in Fig. 13 for different ns^2 mergers. The canonical merger case (thick black line) peaks after 0.4 days with $5 \times 10^{41} \text{ erg/s}$. The macronovae light curves produced by the two nsbh mergers that we consider are depicted in Fig. 14, the canonical ns^2 case ($2 \times 1.4 m_{\odot}$) is shown for reference purposes. Since more mass is ejected these macronovae peak later, at about 0.7 days and their peak luminosities can reach about 10^{42} erg/sec . Our estimates of the macronova peak luminosity for the canonical ns^2 is similar to the calculation of Metzger et al. (2010) for $m_{\text{ej}} = 0.01 m_{\odot}$ and $v = 0.1c$. Other merger cases are brighter by a factor of 2-3 mostly due to the larger amount of ejected mass. Figure 15 show the effect of the opacity on the light curves. Increased opacity delay the peak time ($\propto \kappa^{0.5}$) and reduce its luminosity ($\propto \kappa^{-0.65}$).

A peak luminosity of $\sim 5 \times 10^{41} [10^{42}] \text{ erg}$, that arises in our canonical $\text{ns}^2 [10 m_{\odot} \text{ nsbh}]$ merger, corresponds to an absolute bolometric magnitude of about -15 [-16], or an observed bolometric magnitude of 22 [21] at a distance of $\sim 300 \text{ Mpc}$. The observed magnitude at a given observed optical band, which does not necessarily include the peak of the signal spectrum will be fainter. Thus, a more realistic estimate of the observed luminosity at a distance of $\sim 300 \text{ Mpc}$ is 22.5-23.5[21.5-22.5]. The nsbh macronova bolometric magnitude would be 23.5 at 1 Gpc, roughly the LIGO/Virgo detection horizon for the nsbh merger’s GW signal and at a given optical band it will probably be a magnitude or two fainter. With a rapid

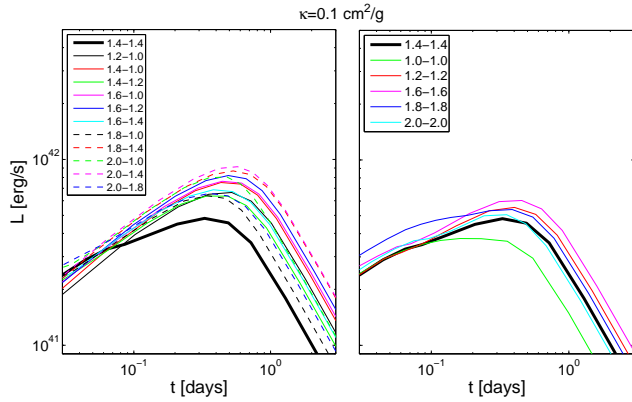


Figure 13. Bolometric light curves of "macronovae" - supernova-like event that are powered by a radioactive decays within the dynamical ejecta. The opacity is assumed to be grey and constant with $\kappa = 0.1 \text{ cm}^2/\text{g}$. Most of the luminosity is emitted in IR, Optical and UV. Left panel: different ns masses; Right panel: equal ns masses. The bold solid black line corresponds to the canonical case of a $1.4\text{-}1.4 m_\odot$ merger.

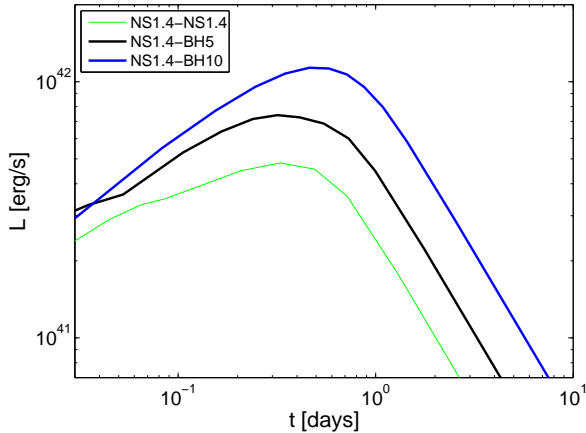


Figure 14. Bolometric light curves of "macronovae" - supernova-like event that are powered by a radioactive decays within the dynamical ejecta. The opacity is assumed to be grey and constant with $\kappa = 0.1 \text{ cm}^2/\text{g}$. Most of the luminosity is emitted in IR, Optical and UV. The lightcurves are for nsbh mergers of different masses. For a comparison the light curve for the canonical $1.4\text{-}1.4 m_\odot$ merger is also shown.

follow-up this can be easily picked up within the duration of 0.4 days by various optical telescopes. However, the large field of view needed to be covered within a short period of time (of order of 100 deg^2) would be very challenging (see discussion by Metzger & Berger 2012). Detection by a blind survey is also possible. Using the PTF limiting magnitude of 21 (Law et al. 2009; Rau et al. 2009) a ns^2 macronova can be detected by the PTF to a distance of $\sim 100 \text{ Mpc}$. The slightly stronger nsbh macronova could be detected to a distance of $\sim 200 \text{ Mpc}$. With a cadence of 5 days only one in twelve ns^2 macronova, that last 0.4 days, will be detected. Taking a covered region of $\sim 2000 \text{ deg}^2$ the expected detection rate is $0.004 \mathcal{R}_{300}$ macronova per year. Detection by the LSST is much more likely. With a full sky coverage at 24.5 magnitude and a cadence of 3 days

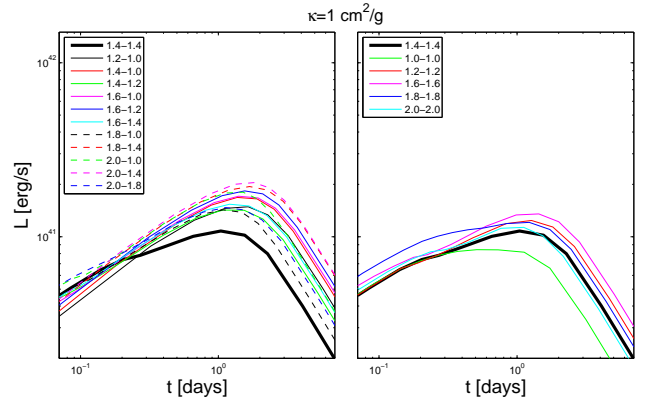


Figure 15. Same as figure 13 with $\kappa = 1 \text{ cm}^2/\text{g}$. The resulting light curves are dimmer and evolving more slowly for larger values of κ .

we expect a LSST horizon for a ns^2 macronova at about 500 Mpc and a detection rate of $\sim 20 \mathcal{R}_{300}$ ns^2 macronovae per year. However, most of those will be observed as single detection transients and identifying their nature is a nontrivial challenge.

6 CONCLUSION

Compact binary mergers are expected to eject sub-relativistic, mildly relativistic and possibly ultra-relativistic outflows. The interaction of such an outflow with the circum-merger environment produces a long-lived radio remnant. Radioactive decay within the outflow produces a short lived IR-UV transient.

To estimate the properties of these transients we have carried out a series of merger simulations which aims at finding the properties of the dynamically ejected mass. This is a lower limit on the amount of the ejected mass, since other sources of sub-, mildly and ultra-relativistic outflows are not accounted for in our simulations, see the discussion at the end of Sec. 2. We find that our canonical merger case of two $1.4 m_\odot$ neutron stars dynamically ejects $0.013 m_\odot$ with a distribution of velocities in the range of $0.05\text{-}0.2 c$ and an average value $\langle v \rangle \approx 0.1c$. The energy carried by this outflow is $1.6 \times 10^{50} \text{ erg}$. Other ns^2 mergers, and especially those with unequal masses, generate more massive outflows at slightly faster velocities, up to $0.04 m_\odot$ and $9 \times 10^{50} \text{ erg}$ of kinetic energy in some cases. The dynamically ejected outflow that we find for nsbh mergers carries about 10^{51} erg .

A strong radio remnant is expected in any merger of a ns^2 whose properties are similar to those of the Galactic neutron star binary population (i.e., typical circum-merger Galactic disk density of 1 cm^{-3}). Such a radio remnant appears months to years after the merger and remains bright for a similar time. Therefore, a trigger following the detection of a GW signal can wait weeks after the event and no online triggering is needed. In addition the long lifetime of the remnants enables their detection in a blind survey. Here we calculate the light curves from one year after the merger,

since our simulations do not include the mildly relativistic outflow which dominates the emission at earlier times. The radio flux from a canonical $1.4\text{--}1.4\ m_{\odot}\ ns^2$ merger taking place at the advanced LIGO/Virgo horizon for such mergers, 300 Mpc, in $n = 1\ \text{cm}^{-3}$ environment is 0.04 mJy (0.2 mJy) at 1.4 GHz (150 MHz) 1-4 years after the merger. This signal could be easily detected by an one hour observation of the EVLA or by a whole day observation on ASKAP or MeerKAT. The sensitivity of present lower frequency detectors, e.g. LOFAR, at 150 MHz, is insufficient for a detection at the advanced LIGO/Virgo horizon. Longer observations (e.g. 10 hours on the EVLA) can detect these mergers even if they are in a lower density environment ($n = 0.1\ \text{cm}^{-3}$). A mildly relativistic component in the ejecta probably increases the brightness and detectability of the signal on time scales of weeks-months. The nsbh GW horizon is farther than the ns^2 GW horizon. Our numerical simulations find that nsbh mergers produce higher energy outflows resulting in larger fluxes. Overall we find that the ELVA detection horizon for nsbh is almost a factor of two larger than the advanced LIGO/Virgo detection horizon.

We find that the optimal frequency to carry out a search for merger remnants is 1.4 GHz. Taking a sub-relativistic outflow with 10^{50} erg and a canonical ns^2 merger rate of $300\ \text{Gpc}^{-3}\ \text{yr}^{-1}$ (and a range of $20 - 2 \times 10^4\ \text{Gpc}^{-3}\ \text{yr}^{-1}$) we expect a detection of ~ 20 (1-1200 correspondingly) radio ns^2 remnants in a 0.1 mJy all sky survey. The expected higher velocity component increases this rate making remnants detectable even in a survey that covers only a small fraction of the sky or that operates at a mJy sensitivity. Thus, a sensitive large field-of-view GHz survey by currently available facilities has a great potential to constrain the rate of binary mergers, information that is of great importance for the design and operation of the advanced GW detectors.

The detectability of the radio transients depends strongly on the circum-merger density, which may be low if the binary has been ejected from its host galaxy before the merger. This uncertainty implies that there may be a fraction of ns^2 mergers, that take place out of the disk of Milky Way-like galaxies, whose radio flares are faint. However our estimates of the detection rate in a blind radio survey are less affected by this uncertainty as our canonical circum-merger density and the expected merger rate are based on the observed Galactic ns^2 binaries, which are all located in the Galactic disk. If there is a population of mergers which take place out of the disk of Milky Way-like galaxies, it will be in addition to the population that we consider here for radio transient blind searches.

These radio transients should be compared with short GRB orphan radio afterglows. These may be produced by compact binary mergers if they are launching also ultra-relativistic outflows. Our estimates of orphan afterglows detectability are based on short GRB observations and are therefore independent of whether short GRBs are binary mergers or not. The main uncertainty in the rate estimates is the GRB beaming factor. We find that assuming $f_b^{-1} = 30$ there are about a dozen orphan afterglows at 0.1 mJy in a single 1.4 GHz whole sky snapshot. These are dominated by relatively energetic short GRBs ($E_{\gamma,iso} \sim 10^{51}$) and their duration is several weeks. If binary mergers are short GRB engines then a GW-triggered event will most likely be of a low energy GRBs, $E_{\gamma,iso} \sim 10^{49}$ erg, and a true energy, after

beaming correction, that is even lower. Their radio orphan afterglow will probably still be detectable in a deep search. However, its variability time scale is short, about a week, so the search should be done promptly.

Our results show the great potential of 1.4 GHz radio transient observations at the sub-mJy level for the detection of ns^2 mergers. On the observational side these predictions provide an excellent motivation for carrying out a whole sky sub-mJy survey using the EVLA or other upcoming radio telescopes. The main source of contamination in such surveys would be radio supernovae and those could be distinguished from compact binary mergers by their optical signal, optically thick spectrum and other characteristic properties.

The IR-UV light curves expected from “macronovae”, supernova-like events powered by the radioactive decay within the ejecta, depends on the total mass ejected and on the velocity distribution. We present a general method for performing such calculations. For each of the 23 simulations that cover the binary parameter space we follow a large number of ejecta trajectories with a state-of-the-art nuclear reaction network. All trajectories show very similar radioactive heating histories which were fitted in Korobkin et al. (2012), see their equation (12). A large uncertainty, though, comes from the poorly known outflow opacity. If we adopt the value that has been discussed in some detail in Metzger et al. (2010), we find that ns^2 [nsbh] mergers peak at about 5×10^{41} [10^{42}] erg/s, corresponding to absolute bolometric magnitudes of -15 [-16]. The magnitude in a given observed optical band is probably fainter by a magnitude or two. Such events can be detected by current blind surveys like PTF up to a distance of about 150 [300] Mpc and by LSST up to 0.8 [1.5] Gpc. The short duration of these events, about 0.4 [0.7] days, may pose problem as it would require very short cadence surveys. Factoring in these limits we expect for the canonical rate of $300\ \text{Gpc}^{-3}\ \text{yr}^{-1}\ ns^2$ mergers a detection of 0.01 macronovae per year by PTF and 100 per year by the LSST. If the opacity is higher than the value suggested by Metzger et al. (2010) then the peak time is delayed while the peak luminosity drops, making the detection of macronova light even harder.

Before concluding we address the relation between mergers the associated radio flares and the short GRBs. While it has not been confirmed it is possible, and maybe even likely, that compact binary mergers are the origin of short GRBs. For that reason we compared “orphan afterglows with radio flares and demonstrated that radio flares are expected to be brighter. It has been claimed Metzger & Berger (2012) that sGRBs arise in large distances from the host galaxies regions and that low density is inferred from modeling of their afterglow. Hence they suggest that if the association of mergers and GRBs is correct this implies that mergers take place in low-density regions and as such their radio flares will be undetectable. However, we know that regardless of the question whether sGRBs are associated with mergers or not, the compact binaries that have been observed in our galaxy are in the galactic disk, namely in high ISM density. Merger rate estimates based on these binaries (Kalogera et al. 2004a,b) suggest a comparable rate of events to the beaming corrected rate inferred from sGRBs. This implies that, while there may (or may not) be a merger population at low-density environment, there must be (regardless of the whether there is a connection to sGRBs) a

large population of the mergers that take place in Milky Way ISM-like density.

We have presented here the detailed methodology for calculation of the two more robust EM transients that should accompany compact binary mergers - radio flares that arise from the interaction of sub- to mildly relativistic outflows with the surrounding matter and macronovae that arise from the radioactive decay of the neutron star matter. We have obtained these estimates from realistic (employing a slew of microphysics ingredients) though Newtonian merger simulations. The major sources of uncertainty in our estimates for radio flares are the fraction of mildly relativistic ejecta (which can only increase the emission) and the surrounding matter density. For the IR-UV macronovae the main uncertainties are the radioactive energy source within the neutron star matter and its opacity. We find that the prospects for detection of both radio flares and the IR-UV macronova are promising by intensive follow up searches following GW signals. Radio flares that last a few months to years have the advantage that they don't require a rapid followup and that the background sky contamination is rather low. Macronovae are more challenging, as they require a large field of view followup within a very short time frame of days or even less and they need to be identified in the crowded optical transient sky. Their advantage is that their emission is independent of the circum-merger environment.

Acknowledgements

We acknowledge the use of the visualization software SPLASH developed by Daniel Price (2007). The presented simulations were performed on the facilities of the Höchstleistungsrechenzentrum Nord (HLRN). S.R.'s research was supported by DFG grant RO-3399, AOBJ-584282. T.P.'s research was supported by an Advanced ERC grant and by the Israeli center for Excellence for High Energy Astrophysics. E.N.'s research was supported by the Israel Science Foundation (grant No. 174/08) and by an IRG.

REFERENCES

- Abadie J., Abbott B. P., Abbott R., Abernathy M., Accadia T., Acernese F., Adams C., Adhikari R., Ajith P., Allen B., et al. 2010, *Classical and Quantum Gravity*, 27, 173001
- Abbott B. P., Abbott R., Adhikari R., Ajith P., Allen B., Allen G., Amin R. S., Anderson S. B., Anderson W. G., Arain M. A., et al. 2009a, *Reports on Progress in Physics*, 72, 076901
- Abbott B. P., Abbott R., Adhikari R., Ajith P., Allen B., Allen G., Amin R. S., Anderson S. B., Anderson W. G., Arain M. A., et al. 2009b, *Phys. Rev. D*, 80, 047101
- Acernese F., Alshourbagy M., Amico P., Antonucci F., Aoudia S., Astone P., Avino S., Baggio L., 2008, *Classical and Quantum Gravity*, 25, 114045
- Arun K. G., Babak S., Berti E., Cornish N., Cutler C., Gair J., Hughes S. A., Iyer B. R., Lang R. N., Mandel I., Porter E. K., Sathyaprakash B. S., Sinha S., Sintes A. M., Trias M., Van Den Broeck C., Volonteri M., 2009, *Classical and Quantum Gravity*, 26, 094027
- Belczynski K., Kalogera V., Rasio F. A., Taam R. E., Zezas A., Bulik T., Maccarone T. J., Ivanova N., 2008, *Ap. J. Supp.*, 174, 223
- Beloborodov A., 2008, *American Institute of Physics Conference Series*, 1054, 51
- Bildsten L., Cutler C., 1992, *ApJ*, 400, 175
- Blandford R. D., Znajek R. L., 1977, *Mon. not. RAS.*, 179, 433
- Chen W. X., Beloborodov A., 2007, *Ap. J.*, 657, 383
- Chevalier R. A., 1982, *Ap. J.*, 258, 790
- Chevalier R. A., 1998, *Ap. J.*, 499, 810
- Chevalier R. A., Fransson C., 2006, *Ap. J.*, 651, 381
- Chevalier R. A., Fransson C., Nymark T. K., 2006, *Ap. J.*, 641, 1029
- Dalal N., Holz D. E., Hughes S. A., Jain B., 2006, *Phys. Rev. D*, 74, 063006
- Davies M., Benz W., Piran T., Thielemann F.-K., 1994, *ApJ*, 431, 742
- Demorest P. B., Pennucci T., Ransom S. M., Roberts M. S. E., Hessels J. W. T., 2010, *Nature*, 467, 1081
- Dessart L., Ott C. D., Burrows A., Rosswog S., Livne E., 2009, *ApJ*, 690, 1681
- Draine B. T., 2011, *Physics of the Interstellar and Inter-galactic Medium*
- Eichler D., Livio M., Piran T., Schramm D. N., 1989, *Nature*, 340, 126
- Frail D. A., Kulkarni S. R., Ofek E. O., Bower G. C., Nakar E., 2012, *Ap. J.*, 747, 70
- Frail D. A., Soderberg A. M., Kulkarni S. R., Berger E., Yost S., Fox D. W., Harrison F. A., 2005, *Ap. J.*, 619, 994
- Frail D. A., Waxman E., Kulkarni S. R., 2000, *Ap. J.*, 537, 191
- Freiburghaus C., Rosswog S., Thielemann F.-K., 1999, *ApJ*, 525, L121
- Gal-Yam A., Ofek E. O., Poznanski D., Levinson A., Waxman E., Frail D. A., Soderberg A. M., Nakar E., Li W., Filippenko A. V., 2006, *Ap. J.*, 639, 331
- Grote H., the LIGO Scientific Collaboration 2008, *Classical and Quantum Gravity*, 25, 114043
- Guetta D., Piran T., 2006, *Astron. & Astrophys.*, 453, 823
- Guetta D., Stella L., 2009, *Astron. & Astrophys.*, 498, 329
- Hawley J. F., Krolik J. H., 2006, *Ap. J.*, 641, 103
- Hoffman R. D., Woosley S. E., Fuller G. M., Meyer B. S., 1996, *ApJ*, 460, 478
- Hughes S. A., Holz D. E., 2003, *Classical and Quantum Gravity*, 20, 65
- Kalogera V., Kim C., Lorimer D. R., Burgay M., D'Amico N., Possenti A., Manchester R. N., Lyne A. G., Joshi B. C., McLaughlin M. A., Kramer M., Sarkissian J. M., Camilo F., 2004b, *Ap. J. Lett.*, 614, L137
- Kalogera V., Kim C., Lorimer D. R., Burgay M., D'Amico N., Possenti A., Manchester R. N., Lyne A. G., Joshi B. C., McLaughlin M. A., Kramer M., Sarkissian J. M., Camilo F., 2004a, *Ap. J. Lett.*, 601, L179
- Kiziltan B., Kottas A., Thorsett S. E., 2010, *ArXiv e-prints*
- Kochanek C., 1992, *ApJ*, 398, 234
- Kochanek C. S., Piran T., 1993, *Ap. J. Lett.*, 417, L17+
- Korobkin O., Rosswog S., Arcons A., Winteler C., 2012, *submitted*
- Kulkarni S. R., 2005, *ArXiv Astrophysics e-prints*
- Lattimer J. M., Prakash M., 2010, *ArXiv e-prints*
- Law N. M., Kulkarni S. R., Dekany R. G., Ofek E. O.,

- Quimby R. M., Nugent P. E., Surace J., Grillmair C. C., Bloom J. S., Kasliwal M. M., Bildsten L., Brown T., Cenko S. B., Ciardi D., Croner E., 2009, *Publications of the Astronomical Society of the Pacific*, 121, 1395
- Lee W. H., Ramirez-Ruiz E., 2007, *New Journal of Physics*, 9, 17
- Levinson A., Ofek E. O., Waxman E., Gal-Yam A., 2002, *Ap. J.*, 576, 923
- Li L., Paczyński B., 1998, *Ap. J. Lett.*, 507, L59
- Li Z., Chevalier R. A., 1999, *Ap. J.*, 526, 716
- Mandel I., O’Shaughnessy R., 2010, *Classical and Quantum Gravity*, 27, 114007
- Metzger B. D., Berger E., 2012, *Ap. J.*, 746, 48
- Metzger B. D., Martínez-Pinedo G., Darbha S., Quataert E., Arcones A., Kasen D., Thomas R., Nugent P., Panov I. V., Zinner N. T., 2010, *Mon. not. RAS.*, 406, 2650
- Metzger B. D., Martínez-Pinedo G., Darbha S., Quataert E., Arcones A., Kasen D., Thomas R., Nugent P., Panov I. V., Zinner N. T., 2010, *MNRAS*, 406, 2650
- Metzger B. D., Piro A., Quataert, E., 2008, *Mon. not. RAS.*, 390, 781
- Monaghan J. J., 2005, *Reports on Progress in Physics*, 68, 1703
- Nakar E., 2007, *Phys. Rep.*, 442, 166
- Nakar E., Gal-Yam A., Fox D. B., 2006, *Ap. J.*, 650, 281
- Nakar E., Piran T., 2011, *Nature*, 478, 82
- Narayan R., Piran T., Shemi A., 1991, *Ap. J. Lett.*, 379, L17
- Ofek E. O., Breslauer B., Gal-Yam A., Frail D., Kasliwal M. M., Kulkarni S. R., Waxman E., 2010, *Ap. J.*, 711, 517
- Ofek E. O., Frail D. A., Breslauer B., Kulkarni S. R., Chandra P., Gal-Yam A., Kasliwal M. M., Gehrels N., 2011, in preparation
- Phinney E. S., 1991, *Ap. J. Lett.*, 380, L17
- Piran T., 2004, *Reviews of Modern Physics*, 76, 1143
- Podsiadlowski P., Langer N., Poelarends A. J. T., Rappaport S., Heger A., Pfahl E., 2004, *ApJ*, 612, 1044
- Rau A., Kulkarni S. R., Law N. M., Bloom J. S., Ciardi D., Djorgovski G. S., Fox D. B., Gal-Yam A., Grillmair C. C., Kasliwal M. M., Nugent P. E., Ofek E. O., 2009, *Publications of the Astronomical Society of the Pacific*, 121, 1334
- Rezzolla L., Baiotti L., Giacomazzo B., Link D., Font J. A., 2010, *Classical and Quantum Gravity*, 27, 114105
- Rhoads J. E., 1997, *Ap. J. Lett.*, 487, L1+
- Roberts L. F., Kasen D., Lee W. H., Ramirez-Ruiz E., 2011, *ApJL*, 736, L21+
- Rosswog S., 2005, *Ap. J.*, 634, 1202
- Rosswog S., 2009, *New Astronomy Reviews*, 53, 78
- Rosswog S., Davies M. B., 2002, *MNRAS*, 334, 481
- Rosswog S., Davies M. B., Thielemann F., Piran T., 2000a, *Astron. & Astrophys.*, 360, 171
- Rosswog S., Davies M. B., Thielemann F.-K., Piran T., 2000b, *A&A*, 360, 171
- Rosswog S., Liebendörfer M., 2003, *MNRAS*, 342, 673
- Rosswog S., Liebendörfer M., Thielemann F., Davies M. B., Benz W., Piran T., 1999, *Astron. & Astrophys.*, 341, 499
- Rosswog S., Nakar E., Piran T., 2012, submitted, Paper I
- Rosswog S., Price D., 2007, *Mon. not. RAS.*, 379, 915
- Rosswog S., Ramirez-Ruiz E., Davies M. B., 2003, *MNRAS*, 345, 1077
- Rosswog S., Ramirez-Ruiz E., Hix W. R., Dan M., 2008, *Computer Physics Communications*, 179, 184
- Rosswog S., Speith R., Wynn G. A., 2004, *MNRAS*, 351, 1121
- Ruffert M., Janka H., 2001, *Astron. & Astrophys.*, 380, 544
- Schwab J., Podsiadlowski P., Rappaport S., 2010, *ApJ*, 719, 722
- Sekiguchi Y., 2011, *Phys. Rev. Lett.*, 107, 5
- Sengupta A. S., the LIGO Scientific Collaboration the Virgo Collaboration 2010, *Journal of Physics Conference Series*, 228, 012002
- Shen H., Toki H., Oyamatsu K., Sumiyoshi K., 1998a, *Nuclear Physics, A* 637, 435
- Shen H., Toki H., Oyamatsu K., Sumiyoshi K., 1998b, *Progress of Theoretical Physics*, 100, 1013
- Shibata M., Taniguchi K., 2011, *Living Reviews in Relativity*, 14, 6
- Smith J. R., LIGO Scientific Collaboration 2009, *Classical and Quantum Gravity*, 26, 114013
- Soderberg A. M., Kulkarni S. R., Berger E., Chevalier R. A., Frail D. A., Fox D. B., Walker R. C., 2005, *Ap. J.*, 621, 908
- Soderberg A. M., Kulkarni S. R., Nakar E., Berger E., Cameron P. B., Fox D. B., Frail D., Gal-Yam A., Sari R., Cenko S. B., Kasliwal M., 2006, *Nature*, 442, 1014
- the LIGO Scientific Collaboration the Virgo Collaboration 2010, *ArXiv e-prints*
- Thorsett S., Chakrabarti D., 1999, *ApJ*, 7512, 288
- Valentim R., Rangel E., Horvath J. E., 2011, *MNRAS*, p. 409
- van den Heuvel E. P. J., 2004, in V. Schoenfelder, G. Lichti, & C. Winkler ed., *5th INTEGRAL Workshop on the INTEGRAL Universe Vol. 552 of ESA Special Publication, X-Ray Binaries and Their Descendants: Binary Radio Pulsars; Evidence for Three Classes of Neutron Stars?*, p. 185
- Waxman E., Kulkarni S. R., Frail D. A., 1998, *Ap. J.*, 497, 288
- Wen L., Chen Y., 2010, *Phys. Rev. D.*, 81, 082001
- Yamamoto T., Shibata M., Taniguchi K., 2008, *Phys. Rev. D.*, 78, 064054